Research Square

Preprints are preliminary reports that have not undergone peer review.
They should not be considered conclusive, used to inform clinical practice,
or referenced by the media as validated information.

# Cathepsin K-Mediated Phenotypic Switching of Pulmonary Artery Smooth Muscle Contributed to the Development of Chronic Stress-related Pulmonary Hypertension in Mice

**Meiping Zhang**
Yanbian University Hospital
**Songzhen Zhao**
Yanbian Hospital: Yanbian University Hospital
**Ran Chen**
Yanbian Hospital: Yanbian University Hospital
**Miao Li**
Yanbian Hospital: Yanbian University Hospital
**Chaoqun Huang**
The First Hospital of Jilin University
**Meiling Piao**
Yanbian Hospital: Yanbian University Hospital
**Mantong Zhao**
Yanbian Hospital: Yanbian University Hospital
**Xueling Yue**
Yanbian Hospital: Yanbian University Hospital
**Jinshun Piao**
Yanbian Hospital: Yanbian University Hospital
**Shangzhi Shu**
The First Hospital of Jilin University Department of Radiology
**Chunzi Jin**
Yanbian Hospital: Yanbian University Hospital
**Xian Wu CHENG**
chengxw0908@163.com

Yanbian University Hospital https://orcid.org/0000-0002-9758-0632

**Research Article**

**Keywords:** cathepsin K, pulmonary arterial hypertension, vascular remodeling, fibrosis, proliferation

**Posted Date:** November 17th, 2026

**DOI:** https://doi.org/10.21203/rs.3.rs-11565789/v1

**License:** This work is licensed under a Creative Commons Attribution 4.0 International License.
Read Full License

*Research Article*

# Cathepsin K-Mediated Phenotypic Switching of Pulmonary Artery Smooth Muscle Contributed to the Development of Chronic Stress-related Pulmonary Hypertension in Mice

Meiping Zhang[1], MD; Songzhen Zhao[1], MD; Ran Chen[1], MD; Miao Li[1], MD; Chaoqun Huang[2], MD, PhD; Meiling Piao[1], MD; Mantong Zhao[1], MD; Xueling Yue[1], PhD; Jinshun Piao[1], BS; Shangzhi Shu[2], MD, PhD; Chunzi Jin[1], MD, PhD; Xian Wu Cheng[1,3]

[1]Jilin Provincial Key Laboratory of Stress and Cardiovascular Disease, Yanbian University, Yanji, Jilin PR 133000, China

[2]Department of Cardiovascular Disease, The First Hospital of Jilin University, Changchun, Jilin PR. 130021, China

[3]Department of Cardiology and Hypertension, The Affiliated Hospital of Yanbian University (Yanbian Hospital), Yanji, Jilin PR 133000, China

**Running title**: CTSK in Stress-Associated PAH

**Total word counts**: Main text (excluding references and figure legends = 5666, Abstract = 248, no. of figures: 7, no. of supplementary figures: 7, no. of tables: 3

**Corresponding authors:**

1. Prof. Xian Wu Cheng, Jilin Provincial Key Laboratory of Stress and Cardiovascular Disease, The Affiliated Hospital of Yanbian University (Yanbian Hospital),1327 Juzijie, Yanji, Jilin PR 133000, China. Email: chengxw@ybu.edu.cn
2. Dr. Shangzhi Shu, Department of Cardiovascular Disease, The First Hospital of Jilin University, Changchun, Jilin PR. 130021, China. Electronic address: shusz22@mails.jlu.edu.cn
3. Prof. Chunzi, Jin, Jilin Provincial Key Laboratory of Stress and Cardiovascular Disease, Yanbian University, China. Email: jianghulin3@cpu.edu.cn

## ABSTRACT

**Aims:** Exposure to chronic psychological stress is a risk factor for metabolic pulmonary artery hypertension (PAH). Given the critical role of lysosomal cathepsin K (CTSK) in human pathobiology, we examined the role of CTSK in stress-related PAH, focusing on TGFβ/TGF-βR2-SMAD2/3 signaling-mediated switching of the phenotypical changes pf pulmonary artery smooth muscle cells (PASMCs).

**Methods and Results:** Eight-week-old male wild-type ($CTSK^{+/+}$) and CTSK-knockout ($CTSK^{-/-}$) mice were subjected to hypoxia ± the tyrosine-kinase inhibitor SU-5416 with or without chronic restraint stress (CRS). Upon model establishment, the right-ventricular systolic pressure and vascular remodeling were quantified by echocardiography, micro-tip pressure sensor catheter, and biological and histomorphometry methods. Single-cell RNA sequencing (scRNA-seq) revealed elevated CTSK expression in PASMCs from idiopathic PAH patients. In mice, hypoxia ± SU-5416 induced CTSK expression and triggered PAH pathology that was markedly exacerbated by superimposed CRS. Genetic deletion of CTSK attenuated key features of PAH, including right-ventricular systolic pressure elevation and vascular remodeling, as well as a shift of PASMCs towards a synthetic phenotype characterized by increased expressions of extracellular-matrix genes (fibronectin, CTSK, and collagen I), a parallel induction of synthetic markers (TGF-β, VIM, and VCAN), and a decrease in contractile genes (SM22α, CNN1, and ATAC2). Mechanistically, CTSK formed a positive-feedback loop with TGF-β–SMAD2/3 signaling. In PASMCs, the silencing of CTSK abolished

hypoxia- and stress-serum-induced cell proliferation and disrupted this loop, whereas CTSK overexpression amplified both.

**Conclusions:** These results identified CTSK as a critical contributor to PAH pathogenesis, particularly under chronic stress conditions. CTSK drives disease progression by enforcing a self-amplifying CTSK–TGF-β–SMAD2/3 circuit that switches PASMC phenotype change and proliferation.

**Key Words:** cathepsin K, pulmonary arterial hypertension, vascular remodeling, fibrosis, proliferation

**Graphic Abstract:** A graphic abstract is available for this article.

## Nonstandard Abbreviations and Acronyms

BMPR2: bone morphogenetic protein receptor 2
BrdU: 5-bromodeoxyuridine
Co-IP: co-immunoprecipitation
Collagen I: collagen type I
CRS: chronic restraint stress
CTSK: cathepsin K
CTSL: cathepsin L
DMEM: Dulbecco's modified Eagle medium
ECM: extracellular matrix
EdU: 5-ethynyl-2-dexyuridine
ELISA: enzyme-linked immunosorbent assay
FBS: fetal bovine serum
GEO: Gene Expression Omnibus
GSDME: gasdermin E
GSEA: gene set enrichment analysis
hPAEC: human pulmonary artery endothelial cell
ICAM-1: intercellular cell adhesion molecule-1
mPAP: mean pulmonary artery pressure
mROS: mitochondrial reactive oxygen species
NS-serum: non-stress-induced serum
ORA: over-representation analysis
PAH: pulmonary arterial hypertension
PASMC: pulmonary arterial smooth cell
PAT: pulmonary artery acceleration time
PBS: phosphate-buffered saline
PET: pulmonary artery ejection time
PPAR-γ: peroxisome proliferator-activated receptor-gamma
RVSP: right ventricular systolic pressure
scGRN: single-cell gene regulatory network
SDS-PAGE: sodium dodecyl sulfate-polyacrylamide gel electrophoresis
siRNA: small interfering RNA
SM22-α: smooth muscle protein 22-alpha
S-serum: stress serum
TGF-β: transforming growth factor-beta
UMAP: Uniform Manifold Approximation and Projection
VCAM-1: vascular cell adhesion molecule-1
VSMC: vascular smooth muscle cell
VTI: velocity–time integral
WA%: wall area percentage
α-SMA: α-smooth muscle actin

# 1. INTRODUCTION

Evidence that has accumulated over the past two decades demonstrates the close association between chronic psychological stress and metabolic and inflammatory diseases, including hypertension, atherosclerosis, obesity, and thrombosis.[1-4] Pulmonary arterial hypertension (PAH) is a heterogeneous, incurable, and ultimately fatal disease characterized by obliterative pulmonary arterial remodeling, which progressively culminates in right ventricular failure.[5-9] A hallmark of PAH is occlusive pulmonary vascular remodeling, which is driven primarily by the excessive proliferation of pulmonary arterial smooth muscle cells (PASMCs),[10] coupled with an aberrant accumulation of extracellular matrix (ECM).[11] Although our research group's recent laboratory studies have shown that chronic psychological stress exerts effects on pulmonary pathologies in animal models,[12] the precise mechanisms by which chronic psychological stress exacerbates PAH remain largely unknown.

Cysteine proteases of the cathepsin family were originally identified as lysosomal and endosomal residents in humans and animals.[13] Their well-recognized core function is proteolysis, which mediates the degradation and recycling of unwanted intracellular or endocytosed proteins within lysosomes.[14, 15] Beyond this canonical role, the cysteine proteases actively contribute to disease pathogenesis by modulating immune and inflammatory responses through ECM remodeling and leukocyte recruitment.[14, 16] Originally identified in osteoclasts, the lysosomal cysteine protease cathepsin K (CTSK) has emerged as a key regulator in cardiovascular pathology, modulating vascular smooth

muscle cell (VSMC) proliferation, neointimal formation, and atherosclerosis.[17, 18] Non-conventional roles of cathepsins have also been suggested in a spectrum of pathologies, including abdominal aortic aneurysms, atherosclerosis, and thrombosis.[1, 19-21] Our laboratory's studies have demonstrated that elevated CTSK levels under chronic stress inhibit the differentiation of adipocytes and promote adipose inflammation.[3] Experimental evidence revealed that CTSK deficiency attenuates kidney damage, fibrosis, and dysfunction under immobilized stress conditions.[22]

Intriguingly, among the cathepsins, a hypermethylation-induced silencing of cathepsin Z primed human pulmonary artery endothelial cells (hPAECs) to inflammation-triggered apoptosis in PAH.[23] Recent evidence further indicates that cathepsin L (CTSL) drives PAH through bone morphogenetic protein receptor 2 (BMPR2)/gasdermin E (GSDME)-mediated pyroptosis,[6] but the role of CTSK in PAH, especially under CPS conditions, remains to be elucidated.

Our present study obtained robust evidence supporting the pathogenic role of CTSK in PAH. To this end, we established hypoxia models with or without the tyrosine-kinase inhibitor SU-5416 using wild-type ($CTSK^{+/+}$) and CTSK-knockout ($CTSK^{-/-}$) mice. The mice were then subjected to either non-stress or chronic restraint stress (CRS) conditions during the final 2 weeks of a 4-week PAH model establishment period. To further elucidate the underlying mechanisms, we exposed PASMCs to hypoxia conditions in the presence of either 5% NS-serum (extracted from the non-stressed mice) or 5% S-serum (extracted from the stressed mice), following CTSK silencing or overexpression.

Taken together, our findings demonstrate that CTSK triggers PASMCs' reprogramming and a self-amplifying CTSK–TGF-β–SMAD2/3 loop that drives PAH vascular remodeling in mice with and without our chronic stress conditions.

## 2. MATERIALS AND METHODS

All data supporting the findings of this study are available from the corresponding authors upon reasonable request. Further details of the study's methods are provided in the Supplementary Information.

### 2.1. Data Mining

The original data mining of single-cell sequencing (scRNA-seq) data in this study from the Gene Expression Omnibus (GEO) GSE169471 was under accession number (GEO Accession viewer),[24] which contains the scRNA-seq data of our study's control groups and idiopathic pulmonary arterial hypertension (IPAH) groups. Healthy controls (GSM5206782, GSM5206783, GSM5206784, GSM5206786, GSM5206788, GSM5206789) and IPAH samples (GSM5206779, GSM5206780, GSM5206781) were selected for analysis. The data processing, exploration, and visualization were completed using the Trailmaker™ platform (https://app.trailmaker.parsebiosciences.com/; Parse Biosciences, Seattle, WA, USA).

After the unfiltered count matrix was uploaded to Trailmaker, the background signal was removed by setting minimum transcript number thresholds (range: 917‑19,909)

for each sample. Dead or dying cells were eliminated by filtering barcodes with a high proportion of mitochondrial genes (range: 0.51%–13.99%). A linear regression model was fitted for the distribution of gene numbers and transcript numbers, and outliers deviating from the model (p-value range: 0.000131–0.000280) were removed. Cells with a high probability of being double cells (range: 0.49–0.74) were identified and removed by the scDblFinder method. After overall filtering, the proportion of retained cells was approx. 92.44%–97.20%.

Using the high-quality cells after screening, we performed data normalization, a principal component analysis (PCA), and data integration analysis based on Harmony. We used the Leiden method to perform a clustering analysis with a resolution value of 0.8, and we calculated the unified flow approximation and projection (UMAP) embedding for the visualization of the results.

### 2.2. Identification of Cell Clusters

The cell type annotations were completed based on the Seurat software package (ver. 5.3.0), using the FindAllMarkers function and the Wilcox statistical method, and by setting the parameters as only.pos = TRUE, logFC = 0.25, and min.pct = 0.25. The cells with similar transcriptomic characteristics were first divided into different clusters, and then the cell type annotations were performed for each cluster based on the expression of recognized marker genes. Cell type marker genes from previous studies were used.[25-28]

### 2.3. Trajectory Analysis

Computationally inferred pseudotime trajectories were constructed with the Monocle3 R package (ver. 1.4.26). The Seurat object was imported into Monocle3 for analysis via the as.cell_data_set function. Smooth muscle cells (SMCs) were used as the starting point for trajectories, and cells were sorted in pseudotime order by using the order_cells function. The dynamic expression changes of genes over pseudotime were then visualized with the plot_genes_in_pseudotime function.

### 2.4. Gene Expression Aggregation and Visualization

Normalized expression values from the RNA assay (i.e., the slot "data") of the Seurat object were extracted at the single-cell level for candidate genes. These values were integrated with metadata containing group assignments and cell-type annotations. For the characterization of expression patterns across conditions, the expression values were aggregated by group within each cell type or experimental condition, and the corresponding average expression levels were computed.

### 2.5. Gene Set Score

The pathway activity per cell was quantified with AUCell (ver. 1.30.1). Genes were ranked within each cell by the expression magnitude (AUCell_buildRankings, default parameters) and queried against curated gene sets compiled from MSigDB, KEGG, and Gene Ontology databases. Area under the curve (AUC) values were calculated with

AUCell_calcAUC and stored in the Seurat object metadata for a downstream analysis. Differential activity between pairs of conditions was assessed by the two-sided Wilcoxon rank-sum test. For multi-group comparisons, the Kruskal–Wallis test was applied first; when the result was significant, pairwise Wilcoxon tests were performed and the p-values were adjusted by the Benjamini–Hochberg (BH) procedure within each gene set.

To determine whether a given cell type exhibited globally elevated or repressed activity, we used one-sample Wilcoxon tests against the genome-wide mean AUC of each signature, again with BH correction. The results are displayed as violin plots superimposed on box plots, with the global mean.

### 2.6. Simulated Specific Knockout of CTSK in SMCs

scTenifoldKnk is a method developed to perform virtual knockout experiments in order to predict gene functions. We applied the specific approach as described.[29] First, scTenifoldKnk, based on scRNA-seq data, constructs a denoised single-cell gene regulatory network (scGRN). The scGRN is copied, and then outward edges of the target gene in the adjacency matrix of the copied scGRN are zeroed out, creating a pseudo-knockout scGRN. By using two scGRNs (one is the initial net and the second is the pseudo-knockout net), the target gene regulatory significance can be estimated with a manifold alignment procedure. Two scGRNs are mapped to the same low-dimensional space, and the distance between gene projections shows the impact of gene knockout in

the scGRN: a larger perturbation of genes in low-dimensional space indicates the importance of the target gene in the scGRN.

In the present study, we applied scTenifoldKnk to the above-mentioned scRNA-seq data, and we performed a simulated knockout of CTSK. The list of perturbed genes was sorted by the fold changes of the distances between the gene projections of the two scGRNs; probabilities were assigned using a $\chi^2$-distribution with one degree of freedom. The most perturbed genes are thought to have a tight connection with the target gene.

### 2.7. GO Enrichment Analysis

A functional enrichment analysis was conducted using the clusterProfiler R package (ver. 4.x), based on the framework of an over-representation analysis (ORA) to statistically evaluate the distribution of gene functions. In this study's ORA analysis, the background gene set (background gene universe) was defined as all the protein-coding genes detected by the RNA assay in the Seurat object, thereby reducing systematic errors introduced by the sequencing depth or detection bias. The GO enrichment analysis focused on the Biological Process ontology. The significance of enrichment of the gene set in each GO entry was evaluated by the hypergeometric test to determine whether the proportion of the target genes in the specific GO entry was significantly higher than the expected proportion in the background gene set. Multiple testing correction was performed using the BH method, and a $q$-value <0.05 after correction was considered significant.

In addition to the ORA enrichment analysis, we performed a gene set enrichment

analysis (GSEA) for the gene perturbation list after virtual knockout. The Z statistic was used as the ranking metric (ranking metric), which comprehensively reflects the perturbation intensity of each gene. All genes were sorted by the absolute value of the Z score from largest to smallest and input into the GSEA function of the clusterProfiler package for the enrichment analysis. The parameters set were: nPermSimple=10000 (10,000 permutations), pAdjustMethod = "BH", minGSSize = 10, and maxGSSize = 500. The gene set was derived from the GO Biological Process database. The enrichment results were summarized with the normalized enrichment score and the corrected FDR (*q*-value), and the corrected significance was used for subsequent sorting and presentation.

### 2.8. Transcription Factor Regulon Analysis

We conducted a single-cell regulatory network inference and clustering (SCENIC)20 analysis to identify the regulatory network and regulon activity of transcription factors (TFs), using the Python module pySCENIC (0.11.2).[30] After running pySCENIC, we obtained a continuous and binary AUC score for each regulation network, where the AUC value represents the regulon activity within the cell cluster. The scaled expression of regulon activity was used to generate a heatmap.

### 2.9. Experimental Animals

The animal experimental procedure was approved by the Ethics Committee on Animal Research at Yanbian University College (Protocol No. YD20240430003).[3] Male CTSK

knockout ($CTSK^{-/-}$, C57BL/6J background) mice were purchased from Shanghai Biomodel Organism Science & Technology Development Co. Male eight-week-old $CTSK^{-/-}$ mice and littermate wildtype ($CTSK^{+/+}$, C57BL/6J) mice were used in the animal experiments. The animals were housed in a 12-hr light/dark cycle (lights off at 19:00) at a controlled temperature of 22 ± 2°C in a pathogen-free facility at the Animal Centre of Yanbian University, with free access to standard food and distilled water. All procedures involving animals were conducted in accordance with the Ethics Committee of Yanbian University and the U.S. National Institutes of Health (NIH) guidelines for the care and use of laboratory animals.

### 2.10. Rodent Models of PAH

Numerical codes were randomly assigned to all of the mice in order to maintain a blinded manner to the testing and analysis of the experimental and control groups. Male $CTSK^{-/-}$ and littermate $CTSK^{+/+}$ mice (aged 8–10 weeks) were exposed to normoxia or hypoxia (10% $O_2$, "Hy") for 4 weeks in a ventilation room with or without an intraperitoneal injection of 20 mg/kg of the tyrosine-kinase inhibitor SU-5416 ("HySU," Sigma-Aldrich, St. Louis, MO, USA), and the construction of the PAH model was conducted as described[31]. From day 1 of hypoxia ± SU-5416 exposure, mice were allocated to either a non-stress regimen or a validated Chronic restraint stress (CRS) paradigm delivered in randomized order as described.[3]

CRS was administered daily for 4 hr from 10:00 a.m. to 2:00 p.m. Specifically, for

the cage tilt stressor, the cage was tilted at a 45° angle for 4 hr. In the isolation paradigm, mice were individually housed in a designated stress cage (cat. no. G-13302; Natsume Seisakusho, Tokyo). For the horizontal caging and damping stressor, sawdust was removed from the cage, water was added, and the cage was suspended horizontally with the mouse's tail submerged in the water for 4 hr. For the overnight lighting stressor, mice were exposed to continuous light from 9 p.m. to 9 a.m. in a separate room.

After PAH was established, its presence was confirmed by echocardiography, hemodynamics, and the observation of right ventricle (RV) hypertrophy. The mice were divided into three experiment groups. For detailed information, see Supplementary Figure S1H and Supplementary Table S1.

### 2.11. Echocardiography

Transthoracic echocardiography was performed with a Vevo 2100 high-resolution ultrasound machine (VisualSonics, Toronto, Canada) with a 30-MHz ultrasound probe for mice.[32] Briefly, the mouse was anesthetized with continuous inhalation isoflurane (3% for induction and 1.5% for maintenance) and placed on a 37°C heated pad in a supine position to obtain an electrocardiogram and the respiratory rate. The chest fur was removed by depilation, ultrasound gel was applied, and the mouse was positioned on a temperature-controlled heating plate set at 37°C with its limbs secured with tape. The heart rate was maintained at 300–500 beats per minute (bpm) whenever possible. The pulmonary artery acceleration time and pulmonary ejection time (PAT/PET) were obtained from the

modified parasternal long-axis view using pulsed-wave Doppler mode, and we calculated the ratio of the PAT to the PET.[33] The tricuspid annulus plain systolic excursion (TAPSE) was examined in the lateral tricuspid annulus near the free RV wall by M-mode from the apical four-chamber view.

### 2.12. Pulmonary Hypertension and the RV Hypertrophy Assay

For right heart catheterization, a closed-chest approach was used. A 1.4-Fr mouse micro-tip pressure sensor catheter (Millar Instruments, Houston, TX) was carefully inserted into the RV to monitor the right ventricular systolic pressure (RVSP). The catheter was connected to a transducer unit interfaced with a signal amplifier and recorder (AD Instruments, Sydney, Australia). The RVSP was then recorded for 5 min until the RVSP reached stability in the mouse, and it was analyzed with Powerlab Pro Software (AD Instruments).[33]

### 2.13. Histological Analysis

Following echocardiogram and catheterization analyses, the mice were euthanized by an overdose of sodium pentobarbital (50 mg/kg) and the tissues and plasma were collected for further analysis. And then each mouse pulmonary circulation was perfused with ice-cold phosphate-buffered saline (PBS) until the lungs turned white. The heart and lungs were then removed. After the dissection and weighing of the RV, the presence and degree of RV hypertrophy was assessed based on the Fulton index, which is calculated as the

weight ratio of the RV divided by the sum of the left ventricle (LV) and septum (LV + S) as described.[5]

After echocardiogram and catheterization analyses, the mice were euthanized by an overdose of sodium pentobarbital (50 mg/kg) and the tissues and plasma were collected for further analysis. The left lung was placed in liquid nitrogen for homogenization, and the lower lobe of the right lung was fixed for 24 hr in 4% paraformaldehyde solution, followed by paraffin embedding and sectioning into 6-μm-thick slices. The medial wall thickness of distal pulmonary vessels was quantified using hematoxylin and eosin (HE) or Masson's staining for a histological analysis according to standard histological staining methods. We quantified the extent of pulmonary vascular remodeling by assessing the medial wall thickness and the degree of muscularization, with the wall area percentage (WA%) of the vascular medial thickness calculated as (total area − luminal area)/total area × 100%.[34] The extent of fibrosis, indicated by blue-green fibrotic tissue areas, was quantified using Image J. All images were captured in a blinded fashion using an EVOS FL Auto 2 imaging system (Thermo Fisher Scientific, Carlsbad, CA) at 40× magnification. A minimum of six animals per group were averaged to quantify positive WA% staining. All measurements were performed blinded to genotype and condition.

### 2.14. Enzyme-Linked Immunosorbent Assays (ELISAs)

Blood plasma was obtained from the mice via cardiac puncture, and the concentration of plasma intercellular adhesion molecule-1 (ICAM-1, cat. no. E-EL-M3037), vascular cell

adhesion molecule-1 (VCAM-1, cat. no. E-EL-M1233) and CTSK (cat. no. E-EL-M0250, Elabscience Biotechnology, Wuhan, China) were determined with an ELISA kit in duplicate according to the manufacturer's instructions.

### 2.15. Immunofluorescence Analysis

Lung sections were deparaffinized in xylene, rehydrated through graded ethanol, and equilibrated in PBS. For oxidative-stress mapping, freshly cut sections were incubated with 10 μM DCFH-DA, a cell-permeable dye (Beyotime, Shanghai, China) at 37°C for 30 min in the dark. For the quantification of medial-wall proliferation, mice were pulsed with 100 mg $kg^{-1}$ BrdU (cat. no. 550891, BD Biosciences, Franklin Lakes, NJ) by intraperitoneal injection 24 hr before lung isolation. Antigen retrieval was performed by microwave heating (2 min) in EDTA buffer; sections were then blocked and stained with a BrdU Labeling and Detection Kit (cat. no. B3035, Applygen, Beijing, China) in mice exposed to hypoxia ± SU-5416 with or without CPS. Lung sections/PASMCs were incubated overnight at 4°C with the indicated primary antibodies: α-SMA (#AF1032, Affinity Biosciences, Cincinnati, OH; 1:400), CTSK (#sc-48353, Santa Cruz Biotechnology, Santa Cruz, CA; 1:200), TGF-βR2 (#sc-17792, Santa Cruz; 1:200), BMPR2 (#ab96826, Abcam. Cambridge, MA; 1:200), CD31 (#ab7388, Abcam, 1:200), phospho-SMAD2/3 (#8828, Cell Signaling Technology, Danvers, MA; 1:400) and collagen I (#ab260043, Abcam, 1:500).

After three washes in PBS-Tween (0.05%), sections were incubated for 2 hr at

room temperature with the following Alexa-Fluor-conjugated secondary antibodies: goat anti-rat IgG (H&L)–FITC (#ab6840, Abcam; 1:500), goat anti-rabbit IgG (H&L)–Alexa 555 (#ab150078, Abcam; 1:500), goat Anti-Mouse IgG H&L-Alexa 647 (#ab150115, Abcam; 1:500), goat anti-rabbit IgG (H+L)–Alexa 488 (#K1206, APExBIO, Houston, TX; 1:500), goat anti-mouse IgG (H+L)–Alexa 488 (#K1204, APExBIO; 1:500) and goat anti-rabbit IgG (H+L)–Alexa Fluor 594 (#S0006, Affinity Biosciences; 1:500). All sections were counterstained with anti-fluorescent quencher within nuclear DAPI (Beyotime Biotechnology, Shanghai, China). Images were acquired using a confocal microscope and analyzed using Image J software. We obtained at least six images of each section at 40× and counted the fluorescence intensity for each section.

### 2.16. Real-time Quantitative Polymerase Chain Reaction (qPCR)

Total RNA samples were obtained from lung tissue using TRIzol reagent (Invitrogen, Carlsbad, CA) according to the recommended protocol. Briefly, total RNA (1 μg) was converted into cDNA using the manufacturer's recommended RT Master Mix (Zomanbio, Beijing, China). The cDNAs were then subjected to a quantitative real-time polymerase chain reaction (qPCR) using a Power SYBR Green PCR Master Mix (Qiagen, Hilden, Germany). An ABI 7300 Real-Time PCR System (Applied Biosystems, Foster City, CA) was used to obtain CT values. Each target gene expression was normalized to GAPDH as the housekeeping gene using the $2^{-\Delta\Delta Ct}$ method, with all experiments performed in triplicate. Supplementary Table S2 summarizes the primer sequences used in this study:

CTSK, TGF-β1, collagen I, ATAC2, calponin-1 (CNN1), smooth muscle protein 22-alpha (SM22-α), versican (VCAN), fibronectin (FN), and vimentin (VIM).

### 2.17. Western Blotting

Lung tissue and cell lysates were prepared using lysis buffer RIPA supplemented with a protease inhibitor and 1% PMSF. The protein concentrations were measured using the Pierce BCA Protein Assay Kit (Solarbio, Beijing, China) at 562 nm on a microplate reader. Equal amounts of proteins were separated by sodium dodecyl sulfate-polyacrylamide gel electrophoresis (SDS-PAGE), transferred to PVDF membranes (Millipore, Bedford, MA) and blocked in 5% milk for 1 hr. Membranes were incubated overnight at 4°C with primary antibodies against CTSK (#sc-48353, Santa Cruz, 1:1,000), anti-transforming growth factor-beta (TGF-β, #3711, Cell Signaling Technology; 1:1,000), anti-peroxisome proliferator-activated receptor-gamma (PPAR-γ, #2435S, Cell Signaling Technology; 1:1,000) and β-tubulin (#ab15246, Abcam; 1:1,000), followed by horseradish peroxidase (HRP)-conjugated secondary antibodies (1:3,000) for 1 hr at room temperature. The Amersham ECL Prime Western Blotting Detection Kit (GE Healthcare, Freiburg, Germany) was then used to determine targeted protein expression using Azure Biosystems software (Azure Biosystems, Dublin, CA), and the levels were normalized by loading β-tubulin levels.

### 2.18. Using the HDOCKER Server for the Prediction of Molecular Docking

Protein structures were sourced from the UniProt database (RRID: SCR_002380; https://www.uniprot.org/) and molecularly docked as described.[35] The complete AlphaFold-predicted structures of CTSK_MOUSE (UniProt ID: P55097) and CTSK_HUMAN (UniProt ID: P43235) were designated as the ligand, whereas those of TGFβR2_MOUSE (UniProt ID: Q62312) and TGFR2_HUMAN (Uniprot ID: P37173) were assigned as the receptor. Docking was performed with the locally installed HDOCKERlite ver. 1.1 platform (RRID: SCR_024799) under default parameters. The subsequent interaction analyses were validated and energetically scored with the PDBePISA platform (RRID:SCR_015749).

### 2.19. Network Pharmacology Analysis

For the network pharmacology analysis, the chemical structure of a TGF-β receptor inhibitor (LY2109761, cat. no. HY-12075, MedChemExpress, Monmouth Junction, NJ) was imported into the Swiss Target Prediction and Super Pred databases for a search for potential TGF-β receptor inhibitor targets. After the removal and merging of duplicates, the results were considered potential targets of TGF-β receptor inhibitor. We also used the keyword phrase "Pulmonary arterial hypertension" to look for disease-related targets in the Gene Cards and DisGeNET databases.

A protein-protein interaction (PPI) network was constructed and analyzed.[4] The intersection of TGF-β receptor inhibitor component targets and PAH-related targets was identified. These intersecting targets were imported into the STRING database with the

species set to Homo sapiens and the minimum required interaction score set to medium confidence (0.400). The resulting TSV file was imported into Cytoscape 3.10.2 for visualization and evaluation. We applied the Network Analyzer plugin to examine topological parameters and targets with a degree value equal to or higher than the mean, and these parameters and targets were refined as the core molecular targets for the TGF-β receptor inhibitor in the management of PAH.

A KEGG pathway enrichment analysis and GO Function analysis were performed as described.[36] In brief, key molecule targets obtained from the intersection of drug and disease targets were imported into the Metascape database for the KEGG pathway enrichment analysis and GO Function analysis. Visualization was achieved by using the Omicshare platform (https://www.omicshare.com/), with the species restricted to a significance threshold of $p<0.05$ and the species set as Homo sapiens. The abundant genes were graded according to their enrichment scores in order to obtain the biological information and functional annotations of the key molecule targets, and we then analyzed the potential mechanisms of the actions of the TGF-β receptor inhibitor in the treatment of PAH.

Molecular docking validation was conducted between CTSK and the TGF-β receptor inhibitor compound (LY2109761). The PDB file for CTSK was downloaded from the Research Collaboratory for Structural Bioinformatics (RCSB) Protein Data Bank (PDB) database (https://www.rcsb.org/), and the protein was dehydrated and processed for small molecules. The 2D structure files (SDF format) of the relevant active

ingredients were downloaded from the PubChem database and converted into the 'mol2' format using ChemDraw software. Molecular docking was then performed using Vina 1.5.6. The protein target and small molecule compounds were processed using AutoDockTools 1.5.6, and molecular docking was performed using Vina 1.5. The molecular docking results were simultaneously visualized and analyzed using PyMOL software.

### 2.20 Co-Immunoprecipitation Assay

For the co-immunoprecipitation assay, mouse lung tissue lysates were prepared in the mixed lysis buffer described above. Protein A/G magnetic beads (#HY-K0202, MedChemExpress, Monmouth Junction, NJ) were pre-conjugated with 5 μg of anti-CTSK mouse antibody, anti-TGF-βR2 rabbit antibody, or matched isotype control IgG (#3900, Cell Signaling Technology) by incubation at 4°C for 1 hr with gentle rotation. Pre-cleared lysates (1 mg) were then added and incubated overnight at 4°C. The beads were sequentially washed with lysis buffer and PBS containing 0.1% Tween-20 (PBST). Eluates were resolved by SDS-PAGE and analyzed by immunoblotting with the indicated antibodies.

### 2.21. Cell Culture

For the cell culture, mouse PASMCs were purchased from Fuheng Biotechnology Co. (Shanghai, China). For hypoxia exposure in vitro, the cells were seeded in culture dishes

and propagated inside a sealed cell incubator maintained at 1% $O_2$ and 5% $CO_2$ at 37°C. After seeding at $2 \times 10^5$ cells per well in six-well plates, the cultures were serum-starved for 6 hr and then exposed for 24 hr to either normoxia (21% $O_2$) or 1% $O_2$ in the presence of 5% NS-serum or 5% S-serum.

In parallel studies, cells were pre-incubated for 30 min with the TGF-β receptor inhibitor LY2109761 (#HY-12075, MedChemExpress) at 10 μM or the CTSK inhibitor balicatib (#B3265, APExBIO) at 1 μM before being subjected to 24 hr of exposure to stress serum-DMEM (Dulbecco's modified Eagle medium) in hypoxia. The lysates were analyzed by western blotting.

### 2.22. CTSK Silencing and Overexpression

For the examination of CTSK silencing and overexpression, PASMCs were transfected with small interfering CTSK RNA (siCTSK), pcDNA-CTSK, or the corresponding negative control, then transiently transfected into PASMCs grown to 70%–80% confluence with the use of Lipofectamine 3000 (Life Technologies, Carlsbad, CA), following the manufacturer's instructions; PASMCs were also molded as described above. The knockdown or overexpression efficiency was determined by the assessment of immunofluorescence or western blotting at 48–72 hr after transfection, followed by cellular assays of targeted protein expression. The siRNA and pcDNA sequences are shown in Supplementary Table S3.

### 2.23. Cell Proliferation Assay

The proliferation of PASMCs was examined by measuring the incorporation of 5-ethynyl-2'-deoxyuridine (EdU) using the BeyoClick™ EdU Cell Proliferation Kit (#C0078S, Beyotime Biotechnology) according to the manufacturer's instructions. Cells were seeded at $2 \times 10^5$ cells per well in six-well plates containing DMEM supplemented with 10% fetal bovine serum (FBS) and then allowed to attach overnight. When the PASMCs cultures reached 70%–80% confluence, the disease model was established as described in sections 2.21 and 2.22. EdU was then added to a final concentration of 10 μM, after which the cells were incubated for 12 hr at 37°C.

After the EdU treatment, the cells were fixed with 4% paraformaldehyde for 15 min at room temperature (RT), permeabilized with Enhanced Immunostaining Permeabilization Buffer (P0097, Beyotime Biotechnology) for 15 min at RT, and incubated with the EdU reaction cocktail for 30 min in the dark. Nuclei were counterstained with the fluorescent DNA stain Hoechst 33342 (1×) for 10 min at RT. Images were acquired using an EVOS FL Auto 2 Imaging System (Thermo Fisher Scientific, Waltham, MA). EdU-positive nuclei were counted and are expressed as a percentage of the total Hoechst-positive nuclei.

### 2.24. Evaluation of Mitochondrial Respiration

For the evaluation of mitochondrial respiration, PASMCs transfected with siCTSK or pl-CTSK were incubated for 24 hr under 21% $O_2$ or 1% $O_2$ with 5% NS-serum or S-serum.

Cells were treated for different purposes before being plated overnight in Seahorse Assay cell culture dishes (Agilent Technologies, Santa Clara, CA). The Agilent Seahorse XFp Analyzer was warmed for >5 hr. Sensor cartridges were hydrated overnight in the calibrant at 37°C without $CO_2$. PASMCs were incubated for 45 min at 37°C before the recording of the oxygen consumption rate (OCR) on an Agilent XFp Analyzer according to the manufacturer's protocol.

### 2.25 PASMC Isolation

Primary PASMCs were extracted from 6- to 8-week-old male $CTSK^{+/+}$ and $CTSK^{-/-}$ mice as described.[31] The protocol applied for the isolation of primary PASMCs is depicted. After the mouse was anesthetized, its thorax was exposed and the first- to third-order intrapulmonary arteries were carefully dissected away from the adipose and connective tissues under an anatomical microscope. Endothelial cells were removed by scraping them off of the endothelial layer. After the adventitia was removed, the isolated pulmonary arteries were digested for 40 min at 37°C. The vessel-derived tissues were then cut into small pieces (1–2 $mm^2$) and explanted in DMEM containing 20% FBS, 100 U $mL^{-1}$ penicillin, and 100 μg $mL^{-1}$ streptomycin at 37°C with 5% $CO_2$. Ten days later, the PASMCs were transferred to a new cell culture dish. PASMCs were identified by immunostaining with an anti-α-SMA antibody.

### 2.26. Statistical Analyses

The data are presented as the mean ± SEM (standard error of the mean) or as the median and interquartile range (IQR) from at least three independent experiments, if not described otherwise. All experiments were performed independently in triplicate. Statistical differences were examined with an unpaired Student's *t*-test (for comparisons of two groups) or a one-way analysis of variance (ANOVA) (for comparisons of three or more groups) followed by Tukey's post hoc tests. The mouse body weight (BW) data were subjected to a two-way repeated measures ANOVA followed by Bonferroni's post hoc tests. The statistical analyses were performed with GraphPad Prism ver. 9.0.0 software (GraphPad, La Jolla, CA). Probability (*p*)-values <0.05 were considered significant. Randomization and blinded analyses were performed whenever possible.

## 3. RESULTS

### 3.1. The Single-Cell Analysis of IPAH Patients Identified a Transitional SMC-Fibroblast State Cluster with Increased CTSK Expression

The GSE169471 dataset was downloaded from the GEO database, and we included the lung tissues of IPAH patients (n=3) and healthy control humans (n=6). A quality control test was performed prior to the test set. We profiled 38,200 single-cell transcriptomes from distal lung explants of control donors and IPAH patients.

To characterize the cellular composition of lung tissue, we performed an unsupervised clustering analysis on single-cell transcriptome data and used UMAP for dimensionality reduction and visualization. At a resolution value of 0.8, the data were

divided into 30 cell clusters (Suppl. Fig. S1A). Based on the expression information of classical markers compiled from the literature in each cluster (Suppl. Fig. S1B), we initially annotated 12 cell types, including immune cell populations such as monocytes/macrophages (Mono_Macro), neutrophils, NK/T cells, and mast cells, as well as major structural cell types such as endothelial cells (Endo), SMCs, fibroblasts (Fibro), alveolar type 2 cells (AT), Club cells, and epithelial cells (Epi) (Fig. 1A).

Notably, in the UMAP space, we also observed a cluster located between SMCs and fibroblasts, which we annotated as the SMC-fibroblast transition cluster (SMC_Fibro_trans), speculating that it may represent a transitional transcriptional state connecting these two mesenchymal cell lineages. In addition to cell clusters defined by cell lineages, we identified a cell cluster characterized by a high expression of cell cycle-related genes and annotated it as cycling cells. This cell cluster is more likely to represent a common proliferative state shared by multiple cell types rather than an independent cell lineage.

To assess the cell composition changes related to IPAH, we compared the relative abundance of major vascular-associated cell populations in the lung tissues of healthy controls and IPAH patients. As shown in Figure 1B, the proportion of fibroblasts in IPAH lung tissues was slightly increased from 3.7% in the control group to 4.4% in the IPAH group; the proportion of vascular SMCs also rose from 1.3% to 1.7%. These results suggest that the mesenchymal cell compartment in IPAH lung tissues undergoes concurrent changes in cellular composition, which may contribute to pulmonary vascular

structural remodeling.

Given that the expression of CTSK was particularly significantly increased, we further evaluated its expression characteristics in different cell types. As shown in Figure 1C, CTSK was mainly enriched and overexpressed in SMCs and fibroblasts, and we observed a marked upregulation in the SMC_Fibro_trans cluster.

We next analyzed ECM synthesis-related genes in the IPAH patients and control subjects. Supplementary Figure S1C shows that the lung tissues of the IPAH patients had increased levels of COL1A1, COL1A2, COL3A1, FN1, VIM, TGFB1, TGFB2, and TGFB3 genes. Interestingly, we scored gene sets at the single-cell level across the entire population and observed that the IPAH lung-derived cells exhibited significantly elevated scores for the gene sets associated with ECM synthesis, hypoxia response, the TGF-β signaling pathway, and the epithelial-mesenchymal transition (EMT) (all $p<0.001$) (Suppl. Fig. S1D–G). These observations indicate that at the single-cell level, the IPAH lungs exhibited overactions in ECM production, the hypoxia response, and pro-fibrotic and mesenchymal programs.

### 3.2. Analysis of the Human IPAH Lung Tissue Cell Subpopulation Maps and Transcriptional Characteristics

To more precisely characterize the heterogeneity of these key cell populations in the IPAH context, we isolated SMCs, fibroblasts, and their transitional states from the whole-cell population. After the dimensionality reduction and the unsupervised clustering analysis

(resolution = 0.2), we identified the five distinct transcriptionally defined cell subpopulations depicted in Figure 1D.

We further systematically compared the expression patterns of SMC and fibroblast-associated marker genes across the five subgroups. A bubble plot analysis revealed significant differences in gene expression between subgroups for contractile function-related genes and ECM-related genes as follows: (*i*) Subgroup 0 and Subgroup 1 simultaneously express smooth muscle cell and fibroblast-related genes; (*ii*) Subgroup 2 had markedly increased ECM-related genes (COL1A2, LUM, and DCN) accompanied by PDGFRA gene overexpression; and (*iii*) Subgroup 3 had markedly elevated classical smooth muscle contraction markers (MYH11, MYLK, MYL9, TAGLN, and ACTA2), supporting their biological positioning as smooth muscle‑fibroblast transitional cells (Fig. 1E).

The further gene set scoring analysis functionally validated the aforementioned phenotypic classification. In collagen biosynthesis-related processes, Subgroup 2 scored significantly higher than the global mean and the other subgroups, suggesting enhanced ECM synthesis potential; conversely, Subgroup 3 scored significantly below the overall level (Fig. 1F). Correspondingly, in smooth muscle contraction-related processes, Subgroup 3 scored significantly above the global mean, indicating a prominent contractile phenotype, while Subgroup 2 showed markedly reduced scores (Fig. 1G). Notably, Subgroup 0 and Subgroup 1 exhibited intermediate levels in both functional scores, with minimal deviation from the global mean. This further supports their functional

classification as smooth muscle‑fibroblast transitional cells. Overall, the functional gradient observed within the nonparametric statistical framework aligns strongly with the transcriptional profiles and marker gene analyses.

To systematically characterize the functional heterogeneity of the smooth muscle‑fibroblast lineage in the context of IPAH, we performed a modular analysis on differentially expressed genes across the five subclusters (C0‑C4, corresponding to subclusters 0‑4) after clustering, and we annotated their functional features using GO biological process enrichment (Fig. 1H). C0 (subgroup 0) showed predominantly enriched gene modules related to stress fiber assembly, suggesting characteristics that are consistent with smooth muscle cells transitioning toward a synthetic phenotype. C1 (subgroup 1) exhibited significantly enriched pathways associated with smooth muscle contraction, indicating that this subgroup retained contractile smooth muscle cell features but exhibited signs of functional remodeling. C2 (subgroup 2) exhibited pronounced expressions of genes related to ECM organization and fibroblast proliferation, suggesting a state closer to fibroblast-like cells with active-matrix synthesis. C3 (subgroup 3) showed enriched modules associated predominantly with actin-mediated cell contraction, representing typical contractile SMCs. In contrast, C4 (subgroup 4) was specifically enriched for processes related to RNA splicing, etc, which suggests that this subgroup may represent a highly active cell population undergoing transcriptional reprogramming.

Based on the integrated transcriptomic features and functional annotation results, we define subgroup 0 and subgroup 1 as smooth muscle–fibroblast transitional SMCs

(trans_SMC1 and SMC2); subgroup 3 was defined as classical contractile SMCs, and subgroup 2 was defined as fibroblasts, whereas subgroup 4, lacking distinct smooth muscle or fibroblast features, was categorized as other_SMCs (Fig. 1I). At the cellular composition level, both the classical SMCs and the fibroblasts showed significantly increased relative proportions in the IPAH group compared to the controls (Fig. 1J).

Conversely, the decreased proportions of trans_SMC1 and transitional cells suggest that in this dataset, the SMC phenotypic conversion may preferentially converge toward terminal states (classical SMCs or fibroblasts), resulting in a relative reduction of transitional cells. Collectively, these findings support a shift from a stable to a remodeled state in vascular wall cells in IPAH, indicating that the expansion of SMCs and fibroblasts may represent a key cellular basis driving pulmonary vascular structural remodeling.

### 3.3. A AdditiveAdditive Induction of CTSK Expression and Pulmonary arterial remodeling in Four Experimental PAH Models

Four groups of $CTSK^{+/+}$ mice were subjected to the following treatments: normoxia (Nor), hypoxia (Hy), hypoxia plus SU-5416 (HySU), or Hypoxia plus SU-5416[37, 38] and the CRS protocol (HySU-S) (Suppl. Fig. S2A). As shown in Supplementary Figure S2B, the quantitative ELISA data demonstrated that the the plasma CTSK concentration was significantly and additively upregulated in mice in response to the Hy, HySU, and HySU-S inductions. Consistent with the CTSK expression, the outcomes of our morphometric analyses confirmed that the pulmonary arteriolar WA% and perivascular fibrosis were

additively enhanced by those PAH induction procedures compared to the respective controls (Suppl. Fig. S2C,D,E). The quantitative right catheterization analysis also revealed elevated RVSP, confirming the successful establishment of the PAH model (Suppl. Fig. S2F,G). Our echocardiography and RV hypertrophy assays also demonstrated an additive harmful change in the PAT/PET ratio, TAPSE, and the Fulton index (i.e., the ratio of the RV to the LV plus septum weight) (Suppl. Fig. S2H–J).

We also observed an additive action on the alterations in the levels of body wight change, subcutaneous adipose weight, and lung weight as well as the gene expressions of the fibroblast-associated ECM synthetic markers (CTSK, TGF-β1, collagen I, VCAN, FN, and VIM) and SMC-associate contraction-related markers (ATAC2, CNN1, and SM22-α) in mice response to our experimental PAH inductions (Suppl. Fig. S2K–P). These results indicate that (*i*) CTSK is a key critical mediator in the development of PAH in mice under our experimental conditions, and (*ii*) CRS is a critical risk factor for this PAH development.

### 3.4. CTSK Is Important in Hypoxia-Induced PAH

To further characterize the phenotypic pulmonary arterial remodeling processes in the context of PAH, we performed a pseudo-temporal trajectory analysis of re-clustered smooth muscle cells, fibroblasts, and their transitional states. In the early stages of the pseudo-temporal trajectory, the cells primarily exhibited the typical contractile SMC transcriptional signatures. As the trajectory progressed, the cells gradually acquired gene

expression programs that are associated with ECM synthesis and fibroblast-like functions (Fig. 2A). CTSK-positive cells accumulate along pseudotime, with a higher proportion of CTSK expressing cells observed in late pseudotemporal cells. (Fig. 2B). This pattern suggests an association between CTSK and a matrix-synthesizing fibroblast-like phenotype.Our GSEA of PASMC-virtual CTSK deletion revealed a downregulation of the collagen-metabolic process, plus cell-adhesion and molecular-fiber-organization modules (Fig. 2C). The running enrichment curves for these pathways peaked at the top of the gene list, with significant corrected *p*-values. These results were further corroborated by the Gene Ontology enrichment for ECM assembly and focal-adhesion pathways (Fig. 2D).

We used both $CTSK^{-/-}$ mice and their littermate controls $CTSK^{+/+}$ mice to investigated the role of CTSK in hypoxia-induced PAH (Fig. 2E). As illustrated in Figure 2F-I, we identified no significant abnormal histological change in the $CTSK^{-/-}$ mice compared to their littermate controls under normoxia. On exposure to hypoxia for 4 weeks, a thinner medial wall, a lesser degree of perivascular fibrosis, and a smaller $BrdU^{+}$/α-$SMA^{+}$ area were present in the $CTSK^{-/-}$ mice (Fig. 2F-I). Consistent with these morphological changes, lowered RVSP and a lower ratio of RV to LV+S (Fig. 2J–L) were observed in the $CTSK^{-/-}$mice compared to the $CTSK^{+/+}$ mice. The echocardiography analysis revealed that hypoxia significantly lowered the TAPSE and PAT/ET in the $CTSK^{+/+}$ mice, and this effect was reversed in the $CTSK^{-/-}$ mice (Fig. 2M,N). Moreover, the CTSK knockout reversed the hypoxia-induced lung TGF-β upregulation and PPAR-γ

downregulation, but not in the normoxia conditions (Fig. 2O). In addition, the hypoxic condition resulted in decreases in the body wight, subcutaneous adipose weight, and increases in lung weight as well as the plasma ICAM-1 and VCAM-1 levels in the $CTSK^{+/+}$ mice, and these effects were rectified by CTSK knockout (Suppl. Fig. S3A–E).

Next, PASMCs were isolated from $CTSK^{+/+}$ and $CTSK^{-/-}$ mice with hypoxia (Suppl. Fig. S3F) and validated by α-SMA immunofluorescence (Suppl. Fig. S3G). The results of the EdU cell proliferation assay demonstrated that CTSK deletion impaired the induction of PASMC proliferation by S-serum/hypoxia (Suppl. Fig. S3H).

### 3.5. CTSK Deletion Attenuated the Stress-Induced PAH in Mice under the HySU Pathological Conditions

A CRS model has often been used to evaluate the impact of chronic psychological stress on metabolic cardiovascular disorders.[1, 21] In the present study, we exposed both $CTSK^{-/-}$ and littermate control $CTSK^{+/+}$ mice to HySU with or without the CRS protocols described in the Methods section (Fig. 3A). On exposure to HySU or HySU-S for 4 weeks, the $CTSK^{+/+}$-HySU mice with CRS exhibited increased the pulmonary arterial WA% and perivascular fibrosis compared to the respective control $CTSK^{+/+}$-HySU mice, and these changes were reversed by CTSK depletion (Fig. 3B–D).

Consistent with the morphological changes, decreased RVSP (Fig. 3E) and a decreased ratio of RV to LV+S (Fig. 3F) were observed in the $CTSK^{-/-}$ mice compared

to those in the $CTSK^{+/+}$ mice. The echocardiography data also confirmed that the application of CRS significantly lowered the PAT/ET and TAPSE value in the $CTSK^{+/+}$ mice, and these effects were rectified by CTSK deletion (Fig. 3G,H). As anticipated, the CTSK knockdown resulted in TGF-β protein downregulation and PPAR-γ protein upregulation in the mice under the HySu or HySU-S conditions (Fig. 3I). Moreover, the qPCR and ELISA data confirmed that CTSK deletion improved the plasma ICAM-1 and VCAM-1 levels (Fig. 3J) as well as the pulmonary arterial remodeling-related gene alterations (CTSK, TGF-β1, collagen 1, ATAC2, CNN1, SM22α, VCAN, FN, and VIM) in the lungs of the mice with HySU- or HySU-S-induced PAH (Fig. 3K–M).

### 3.6. CTSK Gene Modification Modulates the Hypoxia/S-serum-Induced PASMC Phenotype and Proliferation

Considering the critical role of CTSK in the development of PAH in vivo, we first performed mechanistic experiments using PASMCs. As depicted in Supplementary Figure S4A, PASMCs were cultured in hypoxic condition (1% $O_2$) for 24 hr and then subjected to an 5-ethynyl-2-dexyuridine (EdU) assay. Consistent with the in vivo biological actions, the hypoxic stress increased PASMC proliferation ability (Suppl. Fig. S4B–C). Subsequently, with the mimicking in vivo stress condition, PASMCs transfected with siCTSK and control siRNA were cultured in 5% S-serum/hypoxic stress condition for 24 hr (Fig. 4A). We evaluated the siCTSK efficiency in PASMCs by conducting immunofluorescence and immunoblotting assays (Suppl. Fig. S5A,B). As shown in

Figure 4B,C, no significant targeted molecular abnormal change was present in the siCTSK-treated cells compared to the control siRNA-treated cells under the normoxia plus NS-serum condition.

In the S-serum/hypoxic stress conditions, CSTK silencing rectified the TGF-β protein upregulation and increased the PPAR-γ protein downregulation in PASMCs (Fig. 4B,C). The EdU staining assay also confirmed a higher fraction of proliferating cells in siCTSK-treated cells compared to that in the control siRNA-treated cells (Suppl. Fig. S5C,D). The results of the quantitative double immunofluorescence assay and Seahorse assay revealed that CTSK silencing also improved the nuclear p-SMAD2/3 (Fig. 4D, Suppl. Fig. S5E) and intracellular collagen-I accumulation (Fig. 4E, Suppl. Fig. S5F) and mitochondrial respiration dysfunction (basal, ATP-linked, maximal and reserve capacity) in PASMCs compared to the control siRNA (Fig. 4F, Suppl. Fig. S5G–J). These observations indicate that the CTSK silencing-mediated inhibition of cell proliferation might be due to the mitigation of TGF-β overexpression and PPAR-γ-mediated mitochondrial respiration in PASMCs under S-serum/hypoxic stress conditions.

To further confirm the role of increased CTSK in PASMCs, we overexpressed CTSK in PASMCs by using a CTSK-encoding plasmid (plCTSK) and cultured the cells in 5% NS-serum and S-serum under hypoxia (Fig. 5A). We also confirmed the plCTSK efficacity (Suppl. Fig. S6A,B). CTSK overexpression amplified hypoxia with 5% S-serum-induced TGF-β upregulation and PPAR-γ downregulation (Fig. 5B,C), in addition to cell proliferation augmentation (Suppl. Fig. S6C,D), nuclear p-SMAD2/3 (Fig. 5D,

Suppl. Fig. S6E) and intracellular collagen I accumulation (Fig. 5E, Suppl. Fig. S6F), and oxygen consumption reduction (Fig. 5F, Suppl. Fig. S6G–J). These findings further confirm our hypothesis that CTSK regulates the hypoxia+S-serum-induced PASMC phenotype and proliferation.

### 3.8. The Inhibitor of CTSK Attenuated TGF-β Signaling in PASMCs

As illustrated in Supplementary Figure S7A, the PASMCs were cultured in 5% S-serum/hypoxic conditions containing a vehicle or the CTSK inhibitor balicatib. The inhibition of CTSK greatly mitigated the CTSK, TGF-β, and PPAR-γ protein expressions in response to S-serum/hypoxic stress (Suppl. Fig. S7B).

### 3.9. The TGF-β Blockade Mitigated the PASMCs' Proliferation and Collagen Deposition

To clarify how TGF-β signaling governs PASMCs' proliferation, we applied a network pharmacology approach to explore the potential molecular targets of the TGF-β receptor 2 (TGF-βR2) inhibitor LY2109761 for PAH. A total of 245 TGF-βR2 inhibition-related genes in the SwissTargetPrediction database were identified, and 8,183 genes linked to pulmonary hypertension were obtained from the GeneCards database. A Venn diagram generated by the bioinformatics platform revealed 205 overlapping targets (Fig. 6A). To investigate the effects of the TGF-βR2 inhibitor on PAH, we imported the 205 shared molecule targets into the STRING database and constructed a protein-protein interaction

(PPI) network (Fig. 6B) using Cytoscape ver. 3.10.2. The node sizes and colors were adjusted according to degree values, with darker colors indicating higher degrees. CTSK, TGFβR1, and TGFβR2 were identified as high-degree nodes.

A further KEGG enrichment analysis using the DAVID database pinpointed 20 relevant pathways, with a calcium signaling pathway, chemical carcinogenesis-reactive oxygen species, and TGF-β signaling pathways ranking highest (Fig. 6C). As shown in Figure 6D, the results of the gene ontology (GO) pathway enrichment analysis suggested processes associated with the inflammatory response and the regulation of SMC proliferation and migration. Molecular docking predicted the direct binding of the TGF-βR2 inhibitor to CTSK (Fig. 6E).

We next compared lysates from hypoxic cells exposed to 5% stress-serum ± the TGF-βR2 inhibitor LY2109761 (10 μM) (Fig. 6F), and we observed that the treatment with LY2109761 dramatically lowered the S-stress/hypoxia-induced CTSK and TGF-β protein expressions (Fig. 6G, Suppl. Fig. S7C), the nuclear p-SMAD2/3 accumulation (Fig. 6H, Suppl. Fig. S7D), the intracellular collagen-I deposition (Fig. 6I, Suppl. Fig. S7E), and the $EdU^+$ proliferation (Fig. 6J, Suppl. Fig. S7F) while restoring the PPAR-γ protein expression (Fig. 6G, Suppl. Fig. S7C). These data establish a self-amplifying CTSK–TGF-β–SMAD2/3 loop that propagates pulmonary remodeling.

### 3.10. CTSK Bound to TGF-βR2 in PASMCs in Response to Hypoxia with S-serum Exposure

Molecular docking predicted the direct binding of CTSK to TGF-βR2 in both mouse and human proteins (Fig. 7A). To validate this interaction, we performed co-immunoprecipitation (Co-IP) assays. With the use of an anti-CTSK antibody, TGF-βR2 was specifically pulled down from lung tissues of hypoxia-induced PAH mice, whereas in the IgG control there was no binding signal (Fig. 7B). As anticipated, the anti-TGF-βR2 antibody specifically precipitated only CTSK under the same conditions, but not in the control IgG (Fig. 7C). The quantitative immunofluorescent data revealed that S-serum/hypoxic stress increased the co-localization of CTSK with TGF-βR2 in PASMCs; this was reduced by CTSK silencing (Fig. 7D) and increased by its overexpression (Fig. 7E).

To investigate potential transcriptional regulatory differences among the five cell subpopulations, we compared regulon activity profiles across the subpopulations. The AUCell-based regulon activity analysis revealed differentiated regulatory programs between different groups and cell types. Compared to the SMCs, the transcription factor activity for HES1, ELK1, NR2F6, ETV1, IRF8, SP3, RELA and SMAD4 was significantly elevated in the transitional cells (Fig. 7F). SMAD4 activity was significantly enriched in synthetic trans_SMC 1 versus contractile trans_SMC2, pinpointing TGF-β/SMAD signaling as a key driver of phenotypic plasticity.

## 4. DISCUSSION

Our scRNA-seq analysis of IPAH patients revealed that CTSK was enriched and

overexpressed mainly in SMCs and fibroblasts, and we observed a marked upregulation in the SMC_Fibro_trans cluster. We had focused on novel role(s) of CTSK in PASMC phenotypic changes and PAH development in mice under our experimental conditions, and the most significant finding of this investigation is that genetic interventions targeting CTSK were resistant to the development of hypoxia ± SU-5416-induced PAH in mice, especially under the chronic restraint stress conditions. At the molecular, cellular, and morphological levels (in additive manners), CTSK deletion prevented: (*i*) the elevation of CTSK levels in plasma and lung tissues; (*ii*) the elevations of RVSP, the PAT/PET ratio, and the Fulton index and PAPSE reduction; (*iii*) the increasing of the pulmonary arteriolar WA%, perivascular fibrosis, and $CTSK^+$/α-$SMA^+$ cells; and (*iv*) overexpressions of ECM genes (fibronectin, CTSK, and collagen I) and synthetic markers (TGF-β, VIM, and VCAN) and reductions of contractile genes (SM22-α, CNN1, and ATAC2).

In PASMCs, CTSK silencing abolished the hypoxia- and S-serum-induced cell proliferation, and it disrupted TGF-β/TGF-βR2-SMAD2/3 signaling, whereas CTSK overexpression amplified both of these biological actions. In addition, the TGF-βR2 inhibitor LY2109761 blocked the positive feedback loop of CTSK-TGF-β-SMAD2/3, providing evidence and a mechanistic explanation of the activation of CTSK-TGF-β-SMAD2/3 signaling toward the switching of the phenotypic change and proliferation of PASMCs in hypoxia ± SU-5416-induced PAH in mice, especially under the CRS conditions (Fig. 7G).

Members of the cathepsin family have been shown to be overexpressed in stressed

vascular atherogenic plaques, kidney, and adipose tissues.[1, 3, 21] Here we investigated changes in CTSK gene and protein levels in IPAH patients and PAH mice under our experimental conditions. The scRNA-seq revealed elevated CTSK expression in PASMCs from the patients with idiopathic PAH. On day 28 after the stress and PAH inductions (Hy, HySU, and HySU-S), the mice with PAH had increased CTSK protein levels in plasma and lung tissues in a additive manner. Our results demonstrate that the pulmonary arterial remodeling exhibited additive changes, as evidenced by deteriorating hemodynamic parameters (RVSP, PAT/PET, and TAPSE), an increased right ventricular hypertrophy index, vessel wall thickening, and perivascular fibrosis. Because CTSK activity modulates tissue remodeling and fibrosis,[1, 21, 39, 40] we propose that CTSK acts as a crucial mediator of PAH pathogenesis in non-stress and stressed mice.

At the pathological level, IPAH is characterized by a coordinated remodeling of three pulmonary vascular layers: intimal proliferation with chronic inflammation, medial smooth muscle hypertrophy, and adventitial collagen deposition.[41] As is widely acknowledged, PASMCs are a key responder to pulmonary vascular remodeling, contributing both structurally and functionally.[42] As the principal effectors in PAH, PASMCs drive vascular remodeling through dysregulated proliferation, apoptosis resistance, and phenotypic switching.[43] In the present study, the application of hypoxia combined with S-serum markedly induced a proliferation of PASMCs, and CTSK silencing reversed this effect, whereas CTSK overexpression exacerbated it. Our single-cell transcriptome analysis of IPAH lung tissue identified two transitional smooth muscle

cell subpopulations (trans_SMC1 and trans_SMC2), characterized by an upregulation of CTSK that maintains these cells' transitional state and drives extracellular matrix remodeling.

Lineage tracing in mice identified a specific subpopulation of PASMCs that drives neo-muscularization in pulmonary vessels.[44, 45] Consistently, integrated transcriptomic/proteomic atlases revealed that PASMCs execute a phenotypic switch that is characterized by a downregulation of contractile machinery and the induction of ECM biosynthetic programs.[46, 47] Our present experiments identified CTSK as a key regulator of this phenotypic transition, mediating ECM remodeling. The CRS protocols superimposed on hypoxia/SU-5416 exposure amplified the phenotypic switch, characterized by the upregulations of ECM-related genes (CTSK, TGF-β, and collagen I) and synthetic markers (FN, VCAN, and VIM) together with downregulations of contractile markers (CNN1, ATAC2, and SM22α); these changes were reversed by CTSK deletion. These data are consistent with human lung proteomes profiles,[47] suggesting that CTSK regulates transcriptional reprogramming that is associated with pulmonary vascular remodeling in response to hypoxia ± SU-5416, especially under chronic restraint stress conditions.

To establish the associations revealed by single-cell profiling, we developed a novel triple-composite model in CTSK-knockout mice, integrating hypoxia with the tyrosine-kinase inhibitor SU-5416 and chronic restraint stress. It was reported that aberrant TGF-β signaling activation in vascular smooth muscle cells plays a pivotal role

in excessive ECM production.[48] TGF-β signaling, via SMAD activation, is both necessary and sufficient to drive ECM production and progressive tissue fibrosis.[49] Our present findings demonstrated that CTSK deletion inactivated TGF-β signaling and SMAD2/3 phosphorylation, thereby restraining PASMCs' proliferation and collagen I deposition in mice with PAH. Our in vitro experiments revealed mechanistic consistency with our in vivo findings: CTSK silencing or overexpression in PASMCs under hypoxia conditions, with or without serum stimulation, recapitulated the phenotypic changes observed in vivo. These phenotypic changes mirror the pro-fibrotic signature of CTSK-high trans_SMCs identified in single-cell analyses, implicating CTSK in the molecular regulation of SMCs' transition from the contractile phenotype to a synthetic phenotype.

It has been demonstrated that CTSK drives the progression of pulmonary fibrosis by enhancing fibroblast glutamine metabolism and collagen production via a sorting nexin 9 (SNX9)-dependent mechanism that activates the TGF-β1–SMAD3 signaling pathway.[50] In addition, CTSK has been characterized as a proteolytic enzyme that cleaves ECM components and modulates the degradation of insulin receptor substrate 1 (IRS1).[51, 52] However, the precise mechanism by which CTSK regulates TGF-β–SMAD2/3 signaling, whether through proteolytic activity or non-enzymatic pathways, remains to be elucidated.

A 2023 review of multifunctional cysteinyl cathepsins in atherosclerosis-based cardiovascular disease highlighted the finding that CTSK promotes ECM metabolism in both alveolar and interstitial compartments.[13] Moreover, TGF-β–SMAD2/3 signaling

serves as the key regulator of pressure overload-induced fibrotic responses in cardiac fibroblasts via ECM transcription.[53] Our present findings revealed that the combination of stress and hypoxia markedly induces CTSK expression, which in turn activates TGF-β signaling, promotes downstream SMAD2/3 nuclear translocation, and suppresses PPAR-γ expression, leading to collagen I deposition and pro-fibrotic phenotypic switching in PASMCs. In vitro, these effects were significantly reversed by genetic silencing of CTSK and by a pharmacological inhibition of CTSK, whereas CTSK overexpression exacerbated these pathological alterations in cultured PASMCs. Although CTSK is implicated in ECM degradation and lung repair, it has been reported that its high-level expression can function in an extracellular capacity to enhance fibroblast collagen production, thereby contributing to excessive ECM deposition.[50]

A pathological feedback loop has been reported in which the synthetic phenotype promotes ECM remodeling and fibrogenesis, further reinforcing the synthetic state in PASMCs.[54] Our present results indicate that elevated CTSK drives the transition of PASMCs from a contractile to a synthetic phenotype, thereby establishing this feedback loop. Collectively, the upregulation of CTSK/TGF-β signaling by the induction of PAH could represent a common mechanism in PASMCs' phenotypic change and ECM production in mice under our experimental conditions. This process is further amplified by a self-reinforcing PASMC–ECM feedback loop, resulting in pulmonary vascular fibrosis.

An earlier report indicated that TGF-β signaling augments the proteolytic

maturation of pro-CTSK through the regulation of chondroitin 4-sulfate (C4-S) abundance.[55] Accordingly, we investigated this pathway by using the selective TGF-β receptor inhibitor LY2109761 (10 μM) under 1% $O_2$ plus S-serum conditions. The application of LY2109761 blunted the hypoxia-driven CTSK upregulation and SMAD2/3 activation as well as the p-SAMD2/3 nuclear translocation and cell proliferation, while restoring PPAR-γ expression; this result is consistent with our network pharmacology predictions. We validated this interaction through molecular docking, Co-IP, and immunofluorescence assays, the results of which demonstrated that hypoxia enhances CTSK–TGF-βR2 binding, which was further amplified under combined hypoxia (1% $O_2$) and S-serum conditions. Mechanistically, CTSK binding to TGF-βR2 establishes a positive feedback circuit: TGF-β–SMAD2/3 activation drives CTSK transcription, which in turn sustains the pathway activity and amplifies fibrogenesis. In addition, previous studies have demonstrated that the transcriptional regulatory complex formed by SMAD4 and SMAD2/3 is essential for canonical transforming growth factor-β (TGF-β) signaling.[56] Consistent with this finding, nuclear accumulation of the SMAD2/3/4 complex has been shown to orchestrate gene expression programs by directly binding to promoters and recruiting the transcriptional machinery.[57] Our single-cell RNA sequencing–based transcription factor activity analysis revealed markedly enhanced SMAD4 transcriptional activity in the synthetic cluster (trans_SMC1), providing transcriptomic evidence for functional activation of the CTSK–TGF-β/TGF-βR2–SMAD2/3/4 positive feedback loop in a defined cellular state. Mechanistically, binding

of TGF-β to its type I and II serine/threonine kinase receptors triggers phosphorylation of receptor-associated SMAD2/3, which subsequently associates with the common mediator SMAD4 to propagate the signal into the nucleus.[58, 59] Thus, a CTSK–TGF-β/TGF-βR2–SMAD2/3/4 positive-feedback circuit appears to enable a PPAR-γ-mediated proliferation of PASMCs, and this circuit represents a therapeutically tractable axis in PAH.

Mitochondrial reactive oxygen species (mROS) have recently been recognized as integral sensors in PAH as essential stressful mediators,[60] where elevated mROS levels directly drive PASMC proliferation and vascular remodeling.[61] Our research group has demonstrated that CRS increased the expressions of a pro-inflammatory factor (TNF-α) and an oxidative stress marker ($gp91^{phox}$), concomitant with elevated mROS.[3, 36] Our present experiments revealed that this oxidative stress is accompanied by elevated ICAM-1 and VCAM-1 levels in vivo, as well as a reduced oxygen consumption rate under hypoxia conditions in vitro. These effects were further potentiated by CPS/S-serum and reversed by CTSK deletion. Recent evidence implicates immune-cell infiltration and inflammatory-cytokine signaling as key drivers of the pathogenesis of PAH.[62, 63] To our knowledge, these findings are the first to identify CTSK as a trigger of ROS-driven inflammation in PAH, and they establish inhibition of CTSK as a dual-purpose strategy to simultaneously attenuate oxidative injury and inflammatory signaling.

Several limitations of this study should be considered. (1) The CRS model that we used is an animal stress model that cannot completely mimic human psychological stress. The murine model with a combined induction of PAH plus CRS also inherently fails to

completely recapitulate the heterogeneous of human PAH. (2) We could not create a PASMC-specific deletion and overexpression of CTSK in mice to explore the role of CTSK in mice with PAH under our experimental conditions. (3) We could not obtain direct evidence of CTSK binding to TGF-βR2 and the amplification of the CTSK-TGF-SMAD2/3 loop to switch the PASMC phenotypical change and proliferation in the development of experimental PAH. (4) The exclusive use of male mice precluded an assessment of sex-specific effects. Future studies addressing these limitations are warranted.

In summary, CTSK was mainly enriched and overexpressed in PASMCs and fibroblasts, and we observed a dramatic upregulation in the SMC_Fibro_trans cluster in patients with idiopathic PAH. Consistently, we observed a additive induction of CTSK protein expression in our experimental PAH models (Hy, HySU, and HySU-S). The significant amelioration of PAH in the mice with CTSK deletion mice indicates the importance of CTSK in PAH and suggests the possibility that CTSK could be used as a therapeutic molecular target in the prevention and management of PAH.

## In summary

Exposure to chronic psychological stress is a risk factor for metabolic pulmonary artery hypertension (PAH). Our present study revealed that changes in intracellular cathepsin K (CTSK) activity influence the phenotypical change and proliferation of pulmonary artery smooth muscle cells (PASMCs) by regulating transforming growth factor-β/TGF-β

receptor2 (TGF-βR2)-SMAD2/3 signaling activation through a mechanism requiring a positive self-amplifying CTSK–TGF-β–SMAD2/3 loop, thus controlling the development of PAH in mice under our experimental conditions. These findings provide valuable insights into the interplay between intracellular proteolytic CTSK and TGF-β/TGF-βR2-SMAD2/3 signaling in PAH, and they identify CTSK as a critical contributor to PAH pathogenesis, particularly under chronic stress conditions.

## Author Contributions

M. Zhang conceived the project, designed and performed experiments, implemented and analyzed the data, interpreted data, prepared figures, and drafted and wrote the article. S. Zhao, R. Chen, M. Li, C. Huang, M. Piao, M. Zhao, and X. Yue participated in experiments and performed the blinded data analysis of immunostaining. R. Chen performed the scRNA-seq analysis. J. Piao performed the mouse genotyping. S. Shu and C. Jin discussed the results and revised and critically reviewed the article. X.W. Cheng conceived the project, designed and performed experiments, interpreted data, and revised and critically reviewed the article. All authors read and approved the final version of the manuscript.

## Ethical Approval

This study used the publicly available Gene Expression Omnibus (GEO) database. All data were de-identified to comply with the Health Insurance Portability and Accountability Act (HIPAA) Privacy Rule, and no direct patient identifiers were accessible. Additionally, this study was reviewed and approved by the ethics committee.

## Data Availability

The single-cell RNA-seq datasets analyzed in this study are available in the Gene Expression Omnibus (GEO) database under accession number (GSE169471, GEO Accession viewer).

## Acknowledgements

We thank Robert Lafyatis team (BioGDP.com)[64] for the graphical abstract.

## Funding Information

This work was partly supported by grants from the National Natural Science Foundation of China (no. 82370424 to X.W.C), and the Jilin Province Doctoral Sponsorship Project (no. BST202523 to M.Z.), from the Jilin Province Science and Technology Development Plan Project (no. YDZJ202501ZYTS709 to XW.C.; no. YDZJ202501ZYTS232 to X. Y.) and the Jilin Provincial Foundation of Changbai Talent Outstanding Team (no. 20240717129 to X.W.C.).

## Disclosures

The authors declare that they have no conflicts of interest relating to the authorship, research and/or publication of this manuscript.

## Supplementary Material

Supplementary Tables S1–S3

Supplementary Figures S1–S8

## INSTITUTIONAL REVIEW BOARD STATEMENT

The animal study protocols were approved by the Institutional Animal Care and Use Committees of Yanbian University (Protocol No. YD20240430003) and performed in accordance with the Guide for the Care and Use of Laboratory Animals published by the U.S. National Institutes of Health.

## Figure legends

**Fig. 1.** The results of the single-cell RNA-based idiopathic pulmonary arterial hypertension (IPAH) lung tissue cell subpopulation map and the transcriptional feature analysis. **A:** Single-cell RNA-seq UMAP (Uniform Manifold Approximation and Projection) of lung cell populations from control (Ctrl, n=6) and IPAH (n=3) groups. The UMAP of 38,200 single-cell transcriptomes (GSE169471) revealed 12 distinct clusters annotated by classical marker genes. **B:** Cellular composition analysis of healthy controls (*left*, n=24,223 cells) versus IPAH lung tissue (*right*, n=13,977 cells). **C:** Average expression of cathepsin K (CTSK) across major lung tissue cell types, comparing the control and IPAH groups. **D:** UMAP projection of secondary dimensionality reduction and subpopulation segmentation for smooth muscle cells (SMCs), fibroblasts, and their transitional states. **E:** The bubble sizes indicate the proportion of cells expressing the gene (Percent expressed), and the color intensity reflects the average expression levels (Average expression). Among these, MYH11, MYLK, MYL9, TAGLN, and ACTA2 are classic smooth muscle contraction-related genes; COL1A2, LUM, DCN, and BGN are extracellular matrix (ECM) and fibroblast-related genes; PDGFRA is a fibroblast marker gene. **F, G:** GO Biological Process terms for the activity differences in collagen biosynthesis and smooth muscle contraction-related biological processes across distinct smooth muscle‑fibroblast subpopulations. *Dashed lines:* the overall average levels. The overall differences between subpopulations were assessed using the Kruskal–Wallis test. Benjamini–Hochberg (BH)-adjusted $p<0.0001$), ns: no significant difference. **H:**

Differentially expressed gene modules and their functional annotations in the smooth muscle‑fibroblast subpopulations. The heatmap displays the normalized expression levels (Z score) of representative differentially expressed genes (top 10) across five cell subpopulations (C1‑C5) after clustering. Each *row* represents a gene, and each *column* represents a cell subpopulation. *Line graph on the left:* the relative expression trends of each gene module across different subpopulations (gene size = 10). **I:** UMAP projection of the subpopulation annotation results. **J:** Comparison of the cell subpopulation proportions in both groups.

**Fig. 2.** CTSK deletion lowered the hypoxia (Hy)-induced proliferation of pulmonary artery smooth muscle cells (PASMCs) in mice. **A:** The UMAP projection of smooth muscle cells, fibroblasts, and their transitional states after clustering, overlaid with the pseudotime information. Each *point* represents a single cell, with colors transitioning from *purple* (early states) to *yellow* (late states). *Black curve:* inferred developmental/transitional trajectories, with *arrows* pointing in the direction of the overall phenotypic evolution. **B:** The expression dynamics of CTSK during the pseudotemporal progression. Each *point* represents a single cell, colored according to pseudotemporal order, with the *black curve* indicating the fitted trend line. *Vertical axis:* expression values. *Horizontal axis:* the pseudotemporal order. **C:** Perturbation genes identified via the virtual knockout analysis, sorted by the effect statistic Z, followed by a gene set enrichment analysis (GSEA). The figure displays running enrichment curves for

representative GO Biological Process entries. Each curve corresponds to a GO entry, with significance determined via permutation testing and represented by adjusted p-values. **D:** The over-representation analysis (ORA) enrichment analysis of significantly perturbed genes. *Vertical axis:* enriched GO Biological Process entries. *Horizontal axis:* the number of genes enriched in each entry (gene count). The bubble sizes indicate the number of enriched genes. Colors denote the adjusted p-value for multiple testing correction. **E:** The protocol for the mice exposed to normoxia or hypoxia at the indicated time points. **F:** Histological sections stained with hematoxylin and eosin (H&E) (scale bar: 50 μm), Masson staining (scale bar: 50 μm), and for BrdU incorporation (*green:* proliferating cells), α-SMA (*red*) in the four experimental groups of both PAH models. Nuclei were counterstained with DAPI (*blue*). Scale bar: 25 μm. **G–I:** Quantitative data show the area of vascular medial thickness to the total vessel area of pulmonary arteries (H&E), the percentage of fibrosis area (Masson), and the percentage of the $BrdU^+$ to $\alpha\text{-}SMA^+$ in lung tissues of the four groups (n=6/group). **J–N:** Representative images and quantitative data of the right ventricular systolic pressure (RVSP), the right ventricle (RV) divided by the sum of the left ventricle (LV) and septum RV/(LV + S), TAPSE, and PAT/PET in the four experimental groups (n=6/group). **O:** Representative immunoblotting images and quantitative data for the levels of CTSK, TGF-β, and PPAR-γ proteins of the four groups. Data are mean ± SEM. NS: not significant. Statistical significance was assessed by a one-way ANOVA with Tukey's post hoc tests for the data in panels G–I and K–O. TGF-β: transforming growth factor-beta, PPAR-γ: peroxisome proliferator-activated receptor

gamma.

**Fig. 3.** CTSK deletion attenuated the progression of PAH and TGF-β signaling activation in the mice with Hypoxia + SU-5416 (HySU)-induced PAH with or without chronic restraint stress (CRS). **A:** The protocol for the mice exposed to HySU with or without CRS at the indicated time points. **B–D:** Representative immunoblotting images and quantitative data show the area of vascular medial thickness to the total vessel area of pulmonary arteries (H&E), and the percentage of fibrosis area (Masson). Scale bar: 50 μm. **E–H:** Representative images and quantitative data of the RVSP, RV/(LV+S), TAPSE, and PAT/PET in the four experimental groups (n=6/group). **I:** Representative immunoblotting images and quantitative data of CTSK, TGF-β, and PPAR-γ proteins in the four experimental groups (n=4/group). **J:** The plasma concentrations of ICAM-1 and VCAM-1 determined by ELISA (n=7/group). **K‑M:** Real-time quantitative PCR data show the levels of CTSK, TGF-β1, collagen I, VCAN, FN, VIM, ATAC2, CNN1, and SM22α mRNAs in the two experimental groups (n=6/group). Data are mean ± SEM. Statistical significance was assessed by a one-way ANOVA with Tukey's post hoc tests for the data in panels C‑J and an unpaired Student's t-test for the data in panels K‑M. ICAM-1: intercellular cell adhesion molecule-1, PAT: pulmonary artery acceleration time, PET: pulmonary artery ejection time, TAPSE: tricuspid annulus plain systolic excursion, VCAM-1: vascular cell adhesion molecule-1.

**Fig. 4.** CTSK silencing ameliorated hypoxia-induced proliferation of PASMCs in the presence of 5% NS-serum condition or S-serum. **A:** The protocol for the PASMCs transfected with siRNA against CTSK (siCTSK) or non-targeting siRNA (NC) for 48 hr and then exposed to normoxia (21% $O_2$) or hypoxia (1% $O_2$) with 5% NS-serum or S-serum for 24 hr. **B,C:** Representative immunoblotting images and quantitative data of CTSK, TGF-β, and PPAR-γ proteins in the four groups (n=4/group). **D:** Representative immunofluorescent staining images of α-SMA (*green*), p-SMAD2/3 (*red*), and DAPI (*blue*). **E:** Dual immunofluorescence for α-SMA (*green*), collagen I (*red*), and DAPI (*blue*). **F:** The mitochondrial real-time oxygen consumption rate (OCR) measured in the four groups. Scale bar: 10 μm. Data are mean ± SEM. Statistical analysis by a one-way ANOVA with Tukey's post hoc tests for the data in panel C. NC: PASMCs with non-targeting control RNA, si-CTSK: CTSK-silenced PASMCs.

**Fig. 5.** CTSK overexpression amplified the hypoxia-driven proliferation of PASMCs under 5% S-serum. **A:** The protocol for PASMC transfection with the CTSK plasmid (pl-CTSK) and empty plasmid (Cont) for 48 hr; the PASMCs were then exposed to normoxia conditions (21% $O_2$) or hypoxia conditions (1% $O_2$) with 5% NS-serum or 5% S-serum for 24 hr. **B,C:** Representative immunoblots and quantification for the levels of CTSK, TGF-β, and PPAR-γ proteins in the four groups (n=4/group). **D:** Representative immunofluorescent staining images show α-SMA (*green*)-, p-SMAD2/3 (*red*)-, and DAPI (*blue*)-positive staining. **E:** Representative double immunofluorescent images

show α-SMA (*green*)-, collagen I (*red*)-, and DAPI (*blue*)-positive staining. **F:** The mitochondrial real-time oxygen consumption rate (OCR) measured by a Seahorse analyzer. Scale bar: 10 μm. Data are mean ± SEM. For the data in panel C, the statistical analysis was a one-way ANOVA with Tukey's post hoc tests. NC: empty plasmid-treated PASMCs, pl-CTSK: CTSK-overexpressed PASMCs.

**Fig. 6.** The inhibition of TGF-β attenuated the proliferation of PASMCs and the accumulation of collagen I. **A:** A Venn diagram of the TGF-β receptor inhibitor (LY2109761) and pulmonary hypertension, which includes 245 TGF-β receptor inhibitor-related targets (*right*), 8,183 pulmonary hypertension targets (*left*), and 205 overlapping targets (*center*). **B:** The anti-pulmonary hypertension protein-protein interaction (PPI) network. A *larger area* indicates larger nodes, *blue* indicates a closer association, *lighter color* indicates a less close association, and the core target is the target in the *inner circle*. **C:** The KEGG pathway enrichment analysis (DAVID), with the pathways (y-axis), false discovery rate (FDR) (x-axis), and p-values (color change). The bubble size indicates the number of genes enriched in the pathway. **D:** The gene ontology (GO) pathway enrichment analysis. **E:** The molecular docking results of the TGF-β receptor inhibitor with CTSK. **F:** Protocol design: PASMCs were pretreated with or without the TGF-β receptor inhibitor LY2109761 (10 μM, 30 min) prior to 24 hr of hypoxia (1% $O_2$) plus 5% S-serum. **G:** Representative immunoblotting images and quantitative data for CTSK, TGF-β, and PPAR-γ proteins in the two experiment groups (n=3/group). **H:**

Representative immunofluorescence staining of PASMCs treated with or without LY2109761 for α-SMA (*green*), p-SMAD2/3 (*red*), and DAPI (*blue*). Scale bar: 10 μm. **I:** Representative double immunofluorescent images show α-SMA (*green*)-, collagen I (*red*)-, and DAPI (*blue*)-positive staining. Scale bar: 10 μm. **J:** Representative 5-ethynyl-2-dexyuridine (EdU) staining images and quantitative data show the numbers of $EdU^+$ cells (*red*) in both groups. Scale bar: 200 μm.

**Fig. 7.** CTSK bound to TGF-βR2 in PASMCs in response to hypoxia with S-serum exposure. **A:** The in silico model (human/mouse) showing the predicted CTSK–TGF-βR2 binding interface obtained with the HDOCKER server. **B,C:** The results of the co-immunoprecipitation assay using CTSK and TGF-βR2 antibodies to the lung tissues of mice under normoxia and hypoxia conditions. **D:** Representative double immunofluorescent images and quantitative data show CTSK (*green*)-, TGF-βR2 (*red*)-, and DAPI (*blue*)-positive staining in the four groups of CTSK silencing. **E:** Dual immunofluorescence images and quantitative data show CTSK (*green*)-, TGF-βR2 (*red*)-, and DAPI (*blue*)-positive staining in the four groups of CTSK overexpression. Scale bars: 10 μm. **F:** Single-cell regulon activity characteristics of the five subpopulations. **G:** Schematic illustration of the CTSK-TGF-β/TGF-βR2-SMAD2/3/4-positive feedback loop: the signaling drives PASMC remodeling in stress-associated PAH. Data are mean ± SEM. For the data in panels D and E, the *p*-values were determined by a one-way ANOVA with Tukey's post hoc tests.

## REFERENCES


1. Yue X, Piao L, Wang H, Huang Z, Meng X, Sasaki T, Inoue A, Nakamura K, Wan Y, Xu S, Shi GP, Kim W, Murohara T, Kuzuya M and Cheng XW. Cathepsin K Deficiency Prevented Kidney Damage and Dysfunction in Response to 5/6 Nephrectomy Injury in Mice With or Without Chronic Stress. *Hypertension (Dallas, Tex : 1979)*. 2022;79:1713-1723.
2. McAlpine CS, Kiss MG, Rattik S, He S, Vassalli A, Valet C, Anzai A, Chan CT, Mindur JE, Kahles F, Poller WC, Frodermann V, Fenn AM, Gregory AF, Halle L, Iwamoto Y, Hoyer FF, Binder CJ, Libby P, Tafti M, Scammell TE, Nahrendorf M and Swirski FK. Sleep modulates haematopoiesis and protects against atherosclerosis. *Nature*. 2019;566:383-387.
3. Zhang M, Yue X, Xu S, Piao J, Zhao L, Shu S, Kuzuya M, Li P, Hong L, Kim W, Liu B and Cheng XW. Dipeptidyl peptidase-4 disturbs adipocyte differentiation via the negative regulation of the glucagon-like peptide-1/adiponectin-cathepsin K axis in mice under chronic stress conditions. *FASEB journal : official publication of the Federation of American Societies for Experimental Biology*. 2024;38:e23684.
4. Wang H, Zhang M, Xin M, Yue X, Piao J, Zhao L, Bi H, Wang S, Jin C, Nan Y, Jin X and Cheng XW. Dexmedetomidine Reduces Chronic Stress-Related Thrombosis in a Mouse FeCl(3) Model. *FASEB journal : official publication of the Federation of American Societies for Experimental Biology*. 2025;39:e70546.
5. Ranasinghe A, Holohan M, Borger KM, Donahue DL, Kuc RD, Gerig M, Kim A, Ploplis VA, Castellino FJ and Schwarz MA. Altered Smooth Muscle Cell Histone Acetylome by the SPHK2/S1P Axis Promotes Pulmonary Hypertension. *Circulation research*. 2023;133:704-719.
6. Peng Z, Luo XY, Li X, Li Y, Wu Y, Tian Y, Pan B, Petrovic A, Kosanovic D, Schermuly RT, Ruppert C, Günther A, Zhang Z, Qiu C, Li Y, Pu J, Li X and Chen AF. Cathepsin L Promotes Pulmonary Hypertension via BMPR2/GSDME-Mediated Pyroptosis. *Hypertension (Dallas, Tex : 1979)*. 2024;81:2430-2443.
7. Zhou W, Liu K, Zeng L, He J, Gao X, Gu X, Chen X, Jing Li J, Wang M, Wu D, Cai Z, Claesson-Welsh L, Ju R, Wang J, Zhang F and Chen Y. Targeting VEGF-A/VEGFR2 Y949 Signaling-Mediated Vascular Permeability Alleviates Hypoxic Pulmonary Hypertension. *Circulation*. 2022;146:1855-1881.
8. Huang YZ, Wu JC, Lu GF, Li HB, Lai SM, Lin YC, Gui LX, Sham JSK, Lin MJ and Lin DC. Pulmonary Hypertension Induces Serotonin Hyperreactivity and Metabolic Reprogramming in Coronary Arteries via NOX1/4-TRPM2 Signaling Pathway. *Hypertension (Dallas, Tex : 1979)*. 2024;81:582-594.
9. Luo Y, Teng X, Zhang L, Chen J, Liu Z, Chen X, Zhao S, Yang S, Feng J and Yan X. CD146-HIF-1α hypoxic reprogramming drives vascular remodeling and pulmonary arterial hypertension. *Nature communications*. 2019;10:3551.
10. Xu H, Ye L, Du C, Tang H, Zheng Q, Zhu C, Liang B, Wang Y, Mao X, Liang Q,

Zhang J, Shao H, Sun X, Yuan R, Yun W, Luo C, Xiu J, Su W, Fan F, Dai Z, Chen L, Guan Y and Zhang X. EP4/ANXA2 axis in pulmonary arterial hypertension: therapeutic implications. *European heart journal*. 2025.

11. Thenappan T, Ormiston ML, Ryan JJ and Archer SL. Pulmonary arterial hypertension: pathogenesis and clinical management. *BMJ (Clinical research ed)*. 2018;360:j5492.
12. Zhang S, Li P, Xin M, Jin X, Zhao L, Nan Y and Cheng XW. Dipeptidyl peptidase-4 inhibition prevents lung injury in mice under chronic stress via the modulation of oxidative stress and inflammation. *Experimental animals*. 2021;70:541-552.
13. Cheng XW, Narisawa M, Wang H and Piao L. Overview of multifunctional cysteinyl cathepsins in atherosclerosis-based cardiovascular disease: from insights into molecular functions to clinical implications. *Cell & bioscience*. 2023;13:91.
14. Xiao Y, Cong M, Li J, He D, Wu Q, Tian P, Wang Y, Yang S, Liang C, Liang Y, Wen J, Liu Y, Luo W, Lv X, He Y, Cheng DD, Zhou T, Zhao W, Zhang P, Zhang X, Xiao Y, Qian Y, Wang H, Gao Q, Yang QC, Yang Q and Hu G. Cathepsin C promotes breast cancer lung metastasis by modulating neutrophil infiltration and neutrophil extracellular trap formation. *Cancer cell*. 2021;39:423-437.e7.
15. Leng YP, Ma YS, Li XG, Chen RF, Zeng PY, Li XH, Qiu CF, Li YP, Zhang Z and Chen AF. l-Homocysteine-induced cathepsin V mediates the vascular endothelial inflammation in hyperhomocysteinaemia. *British journal of pharmacology*. 2018;175:1157-1172.
16. Fang W, He A, Xiang MX, Lin Y, Wang Y, Li J, Yang C, Zhang X, Liu CL, Sukhova GK, Barascuk N, Larsen L, Karsdal M, Libby P and Shi GP. Cathepsin K-deficiency impairs mouse cardiac function after myocardial infarction. *Journal of molecular and cellular cardiology*. 2019;127:44-56.
17. Fang F, Ni Y, Yu H, Yin H, Yang F, Li C, Sun D, Pei T, Ma J, Deng L, Zhang H, Wang G, Li S, Shen Y and Liu X. Inflammatory endothelium-targeted and cathepsin responsive nanoparticles are effective against atherosclerosis. *Theranostics*. 2022;12:4200-4220.
18. Hu L, Cheng XW, Song H, Inoue A, Jiang H, Li X, Shi GP, Kozawa E, Okumura K and Kuzuya M. Cathepsin K activity controls injury-related vascular repair in mice. *Hypertension (Dallas, Tex : 1979)*. 2014;63:607-15.
19. Qin Y, Cao X, Guo J, Zhang Y, Pan L, Zhang H, Li H, Tang C, Du J and Shi GP. Deficiency of cathepsin S attenuates angiotensin II-induced abdominal aortic aneurysm formation in apolipoprotein E-deficient mice. *Cardiovascular research*. 2012;96:401-10.
20. Jiang H, Cheng XW, Shi GP, Hu L, Inoue A, Yamamura Y, Wu H, Takeshita K, Li X, Huang Z, Song H, Asai M, Hao CN, Unno K, Koike T, Oshida Y, Okumura K, Murohara T and Kuzuya M. Cathepsin K-mediated Notch1 activation contributes to neovascularization in response to hypoxia. *Nature communications*. 2014;5:3838.
21. Xu S, Piao L, Wan Y, Huang Z, Meng X, Inoue A, Wang H, Yue X, Jin X, Shi GP, Kuzuya M and Cheng XW. CTSS Modulates Stress-Related Carotid Artery Thrombosis in a Mouse FeCl(3) Model. *Arteriosclerosis, thrombosis, and vascular*

*biology*. 2023;43:e238-e253.

22. Jin X, Yue X, Huang Z, Meng X, Xu S, Wu Y, Wan Y, Inoue A, Narisawa M, Hu L, Shi GP, Umegaki H, Murohara T, Lei Y, Kuzuya M and Cheng XW. Cathepsin K deficiency prevented stress-related thrombosis in a mouse FeCl(3) model. *Cellular and molecular life sciences : CMLS*. 2024;81:205.
23. Ulrich A, Wu Y, Draisma H, Wharton J, Swietlik EM, Cebola I, Vasilaki E, Balkhiyarova Z, Jarvelin MR, Auvinen J, Herzig KH, Coghlan JG, Lordan J, Church C, Howard LS, Pepke-Zaba J, Toshner M, Wort SJ, Kiely DG, Condliffe R, Lawrie A, Gräf S, Morrell NW, Wilkins MR, Prokopenko I and Rhodes CJ. Blood DNA methylation profiling identifies cathepsin Z dysregulation in pulmonary arterial hypertension. *Nature communications*. 2024;15:330.
24. Saygin D, Tabib T, Bittar HET, Valenzi E, Sembrat J, Chan SY, Rojas M and Lafyatis R. Transcriptional profiling of lung cell populations in idiopathic pulmonary arterial hypertension. *Pulmonary circulation*. 2020;10.
25. Asosingh K, Comhair S, Mavrakis L, Xu W, Horton D, Taylor I, Tkachenko S, Hu B and Erzurum S. Author Correction: Single-cell transcriptomic profile of human pulmonary artery endothelial cells in health and pulmonary arterial hypertension. *Scientific reports*. 2021;11:21086.
26. Jiang P, Huang H, Xie M, Liu Z, Jiang L, Shi H, Wu X, Hao S and Li S. Single-cell characterization of the immune heterogeneity of pulmonary hypertension identifies novel targets for immunotherapy. *BMC immunology*. 2025;26:5.
27. Crnkovic S, Valzano F, Fließer E, Gindlhuber J, Thekkekara Puthenparampil H, Basil M, Morley MP, Katzen J, Gschwandtner E, Klepetko W, Cantu E, Wolinski H, Olschewski H, Lindenmann J, Zhao YY, Morrisey EE, Marsh LM and Kwapiszewska G. Single-cell transcriptomics reveals skewed cellular communication and phenotypic shift in pulmonary artery remodeling. *JCI insight*. 2022;7.
28. Li Y, Zhang YT, Han B, Xue L, Wei Y and Li G. Single-cell sequencing analysis confirms the association of ANRIL with the increased smooth muscle cell proliferation and migration gene signatures in pulmonary artery hypertension in silico. *Advances in medical sciences*. 2024;69:217-223.
29. Osorio D, Zhong Y, Li G, Xu Q, Yang Y, Tian Y, Chapkin RS, Huang JZ and Cai JJ. scTenifoldKnk: An efficient virtual knockout tool for gene function predictions via single-cell gene regulatory network perturbation. *Patterns (New York, NY)*. 2022;3:100434.
30. Aibar S, González-Blas CB, Moerman T, Huynh-Thu VA, Imrichova H, Hulselmans G, Rambow F, Marine JC, Geurts P, Aerts J, van den Oord J, Atak ZK, Wouters J and Aerts S. SCENIC: single-cell regulatory network inference and clustering. *Nature methods*. 2017;14:1083-1086.
31. Rong W, Liu C, Li X, Wan N, Wei L, Zhu W, Bai P, Li M, Ou Y, Li F, Wang L, Wu X, Liu J, Xing M, Zhao X, Liu H, Zhang H and Lyu A. Caspase-8 Promotes Pulmonary Hypertension by Activating Macrophage-Associated Inflammation and

IL-1β (Interleukin 1β) Production. *Arteriosclerosis, thrombosis, and vascular biology*. 2022;42:613-631.

32. Fang J, Shu S, Dong H, Yue X, Piao J, Li S, Hong L and Cheng XW. Histone deacetylase 6 controls cardiac fibrosis and remodelling through the modulation of TGF-β1/Smad2/3 signalling in post-infarction mice. *Journal of cellular and molecular medicine*. 2024;28:e70063.
33. Bian JS, Chen J, Zhang J, Tan J, Chen Y, Yang X, Li Y, Deng L, Chen R and Nie X. ErbB3 Governs Endothelial Dysfunction in Hypoxia-Induced Pulmonary Hypertension. *Circulation*. 2024;150:1533-1553.
34. Zhou JJ, Li H, Li L, Li Y, Wang PH, Meng XM and He JG. CYLD mediates human pulmonary artery smooth muscle cell dysfunction in congenital heart disease-associated pulmonary arterial hypertension. *J Cell Physiol*. 2021;236:6297-6311.
35. Mijit A, Wang X, Li Y, Xu H, Chen Y and Xue W. Mapping synthetic binding proteins epitopes on diverse protein targets by protein structure prediction and protein-protein docking. *Computers in biology and medicine*. 2023;163:107183.
36. Zhang M, Wang H, Li X, Shu S, Piao J, Yue X, Zhao S, Li M, Jin X, Nan Y and Cheng XW. Increased Dipeptidyl Peptidase-4 Promotes Adipose Inflammation and Dysfunction in Mice Under Chronic Stress. *FASEB journal : official publication of the Federation of American Societies for Experimental Biology*. 2025;39:e70893.
37. Ma Q, Yang Q, Xu J, Sellers HG, Brown ZL, Liu Z, Bordan Z, Shi X, Zhao D, Cai Y, Pareek V, Zhang C, Wu G, Dong Z, Verin AD, Gan L, Du Q, Benkovic SJ, Xu S, Asara JM, Ben-Sahra I, Barman S, Su Y, Fulton DJR and Huo Y. Purine synthesis suppression reduces the development and progression of pulmonary hypertension in rodent models. *European heart journal*. 2023;44:1265-1279.
38. Liu G, Wan N, Liu Q, Chen Y, Cui H, Wang Y, Ren J, Shen X, Lu W, Yu Y, Shen Y and Wang J. Resolvin E1 Attenuates Pulmonary Hypertension by Suppressing Wnt7a/β-Catenin Signaling. *Hypertension (Dallas, Tex : 1979)*. 2021;78:1914-1926.
39. Ma L, Lu B, Si Y, Dai L, Tan M, Liu W, Sun D, Shu J, Chen C, Xiang Q, Jiang D, Wei X and Wang WE. Cathepsin K as a key regulator of myocardial fibrosis in dilated cardiomyopathy and a promising therapeutic target. *The Journal of biological chemistry*. 2025;301:110421.
40. Guo R, Hua Y, Ren J, Bornfeldt KE and Nair S. Cardiomyocyte-specific disruption of Cathepsin K protects against doxorubicin-induced cardiotoxicity. *Cell death & disease*. 2018;9:692.
41. Mocumbi A, Humbert M, Saxena A, Jing ZC, Sliwa K, Thienemann F, Archer SL and Stewart S. Pulmonary hypertension. *Nature reviews Disease primers*. 2024;10:1.
42. Zhang Y, Hernandez M, Gower J, Winicki N, Morataya X, Alvarez S, Yuan JX, Shyy J and Thistlethwaite PA. JAGGED-NOTCH3 signaling in vascular remodeling in pulmonary arterial hypertension. *Science translational medicine*. 2022;14:eabl5471.
43. Wu Z, Zhu L, Nie X, Wei L and Qi Y. USP15 promotes pulmonary vascular

remodeling in pulmonary hypertension in a YAP1/TAZ-dependent manner. *Experimental & molecular medicine*. 2023;55:183-195.
44. Sheikh AQ, Saddouk FZ, Ntokou A, Mazurek R and Greif DM. Cell Autonomous and Non-cell Autonomous Regulation of SMC Progenitors in Pulmonary Hypertension. *Cell reports*. 2018;23:1152-1165.
45. Sheikh AQ, Misra A, Rosas IO, Adams RH and Greif DM. Smooth muscle cell progenitors are primed to muscularize in pulmonary hypertension. *Science translational medicine*. 2015;7:308ra159.
46. Crnkovic S, Marsh LM, El Agha E, Voswinckel R, Ghanim B, Klepetko W, Stacher-Priehse E, Olschewski H, Bloch W, Bellusci S, Olschewski A and Kwapiszewska G. Resident cell lineages are preserved in pulmonary vascular remodeling. *The Journal of pathology*. 2018;244:485-498.
47. Régent A, Ly KH, Lofek S, Clary G, Tamby M, Tamas N, Federici C, Broussard C, Chafey P, Liaudet-Coopman E, Humbert M, Perros F and Mouthon L. Proteomic analysis of vascular smooth muscle cells in physiological condition and in pulmonary arterial hypertension: Toward contractile versus synthetic phenotypes. *Proteomics*. 2016;16:2637-2649.
48. Akhurst RJ. TGF beta signaling in health and disease. *Nature genetics*. 2004;36:790-2.
49. Hu HH, Chen DQ, Wang YN, Feng YL, Cao G, Vaziri ND and Zhao YY. New insights into TGF-β/Smad signaling in tissue fibrosis. *Chemico-biological interactions*. 2018;292:76-83.
50. Chen M, Meng X, Zhu Y, Wang D, Wang M, Wang Z, Tian X, Zhang J, Yue Z, Yang Z and Wang R. Cathepsin K Aggravates Pulmonary Fibrosis Through Promoting Fibroblast Glutamine Metabolism and Collagen Synthesis. *Advanced science (Weinheim, Baden-Wurttemberg, Germany)*. 2025:e13017.
51. Meng X, Huang Z, Inoue A, Wang H, Wan Y, Yue X, Xu S, Jin X, Shi GP, Kuzuya M and Cheng XW. Cathepsin K activity controls cachexia-induced muscle atrophy via the modulation of IRS1 ubiquitination. *Journal of cachexia, sarcopenia and muscle*. 2022;13:1197-1209.
52. Dey G, Sinai-Turyansky R, Yakobovich E, Merquiol E, Loboda J, Sridharan N, Houri-Haddad Y, Polak D, Yona S, Turk D, Wald O and Blum G. Development and Application of Reversible and Irreversible Covalent Probes for Human and Mouse Cathepsin-K Activity Detection, Revealing Nuclear Activity. *Advanced science (Weinheim, Baden-Wurttemberg, Germany)*. 2024;11:e2401518.
53. Khalil H, Kanisicak O, Prasad V, Correll RN, Fu X, Schips T, Vagnozzi RJ, Liu R, Huynh T, Lee SJ, Karch J and Molkentin JD. Fibroblast-specific TGF-β-Smad2/3 signaling underlies cardiac fibrosis. *The Journal of clinical investigation*. 2017;127:3770-3783.
54. Crnkovic S, Thekkekara Puthenparampil H, Mulch S, Biasin V, Radic N, Wilhelm J,

Bartkuhn M, Bonyadi Rad E, Wawrzen A, Matzer I, Mitra A, Leib RD, Nagy BM, Sahu-Osen A, Valzano F, Bordag N, Evermann M, Hoetzenecker K, Olschewski A, Ljubojevic-Holzer S, Wygrecka M, Stenmark K, Marsh LM, de Jesus Perez V and Kwapiszewska G. Adventitial fibroblasts direct smooth muscle cell-state transition in pulmonary vascular disease. *eLife*. 2025;13.

55. Flanagan-Steet H, Christian C, Lu PN, Aarnio-Peterson M, Sanman L, Archer-Hartmann S, Azadi P, Bogyo M and Steet RA. TGF-ß Regulates Cathepsin Activation during Normal and Pathogenic Development. *Cell reports*. 2018;22:2964-2977.
56. Zhao B, Yu X, Shi J, Ma S, Li S, Shi H, Xia S, Ye Y, Zhang Y, Du Y and Wang Q. A stepwise mode of TGFβ-SMAD signaling and DNA methylation regulates naïve-to-primed pluripotency and differentiation. *Nature communications*. 2024;15:10123.
57. Massagué J, Seoane J and Wotton D. Smad transcription factors. *Genes & development*. 2005;19:2783-810.
58. Tzavlaki K and Moustakas A. TGF-β Signaling. *Biomolecules*. 2020;10.
59. Wieteska Ł, Taylor AB, Punch E, Coleman JA, Conway IO, Lin YF, Byeon CH, Hinck CS, Krzysiak T, Ishima R, López-Casillas F, Cherepanov P, Bernard DJ, Hill CS and Hinck AP. Structures of TGF-β with betaglycan and signaling receptors reveal mechanisms of complex assembly and signaling. *Nature communications*. 2025;16:1778.
60. Sommer N, Alebrahimdehkordi N, Pak O, Knoepp F, Strielkov I, Scheibe S, Dufour E, Andjelković A, Sydykov A, Saraji A, Petrovic A, Quanz K, Hecker M, Kumar M, Wahl J, Kraut S, Seeger W, Schermuly RT, Ghofrani HA, Ramser K, Braun T, Jacobs HT, Weissmann N and Szibor M. Bypassing mitochondrial complex III using alternative oxidase inhibits acute pulmonary oxygen sensing. *Science advances*. 2020;6:eaba0694.
61. Chen J, Zhang M, Liu Y, Zhao S, Wang Y, Wang M, Niu W, Jin F and Li Z. Histone lactylation driven by mROS-mediated glycolytic shift promotes hypoxic pulmonary hypertension. *Journal of molecular cell biology*. 2023;14.
62. Agrawal V, Kropski JA, Gokey JJ, Kobeck E, Murphy MB, Murray KT, Fortune NL, Moore CS, Meoli DF, Monahan K, Ru Su Y, Blackwell T, Gupta DK, Talati MH, Gladson S, Carrier EJ, West JD and Hemnes AR. Myeloid Cell Derived IL1β Contributes to Pulmonary Hypertension in HFpEF. *Circulation research*. 2023;133:885-898.
63. Zhakeer G, Zeng Y, E G, Maimaitiaili N, Ju P, Yao H, Shi Y, Zhai M, Li K, Zhuang J, Cao Y, Yu Q and Peng W. T(reg) Cells Attenuate Pulmonary Venous Remodeling in PH-LHD via NLRC3 Signaling. *Circulation research*. 2025;136:e113-e128.

64. Jiang S, Li H, Zhang L, Mu W, Zhang Y, Chen T, Wu J, Tang H, Zheng S, Liu Y, Wu Y, Luo X, Xie Y and Ren J. Generic Diagramming Platform (GDP): a comprehensive database of high-quality biomedical graphics. *Nucleic acids research*. 2025;53:D1670-d1676.

# Figure 1

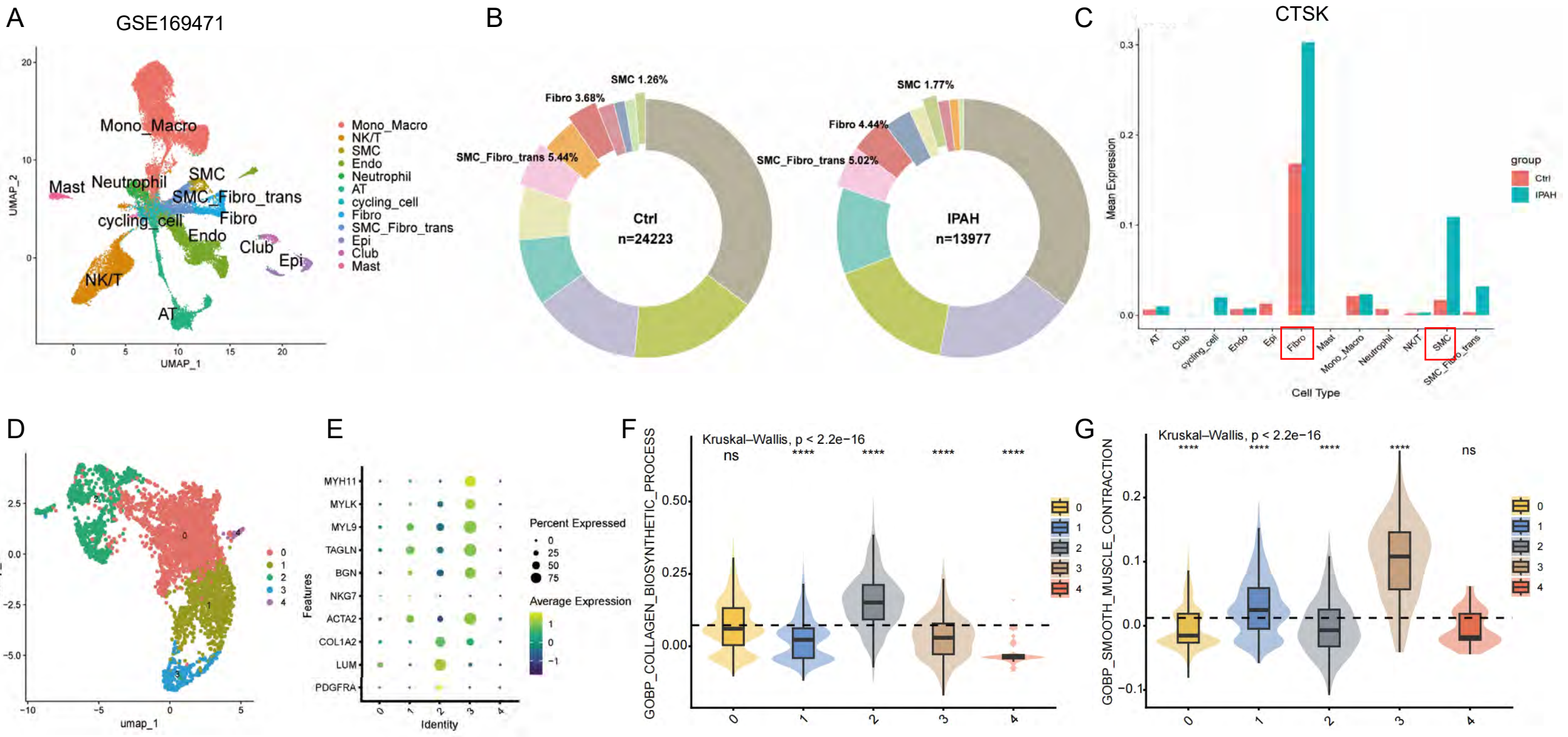

A
GSE169471
Mono_Macro
NK/T
SMC
Endo
Neutrophil
AT
cycling_cell
Fibro
SMC_Fibro_trans
Epi
Club
Mast
UMAP_1
UMAP_2
B
SMC 1.26%
Fibro 3.68%
SMC_Fibro_trans 5.44%
Ctrl
n=24223
SMC 1.77%
Fibro 4.44%
SMC_Fibro_trans 5.02%
IPAH
n=13977
C
CTSK
Mean Expression
group
Ctrl
IPAH
Cell Type
D
umap_1
umap_2
E
MYH11
MYLK
MYL9
TAGLN
BGN
NKG7
ACTA2
COL1A2
LUM
PDGFRA
Features
Identity
Percent Expressed
Average Expression
F
Kruskal–Wallis, p < 2.2e−16
GOBP_COLLAGEN_BIOSYNTHETIC_PROCESS
G
Kruskal–Wallis, p < 2.2e−16
GOBP_SMOOTH_MUSCLE_CONTRACTION

Figure 1

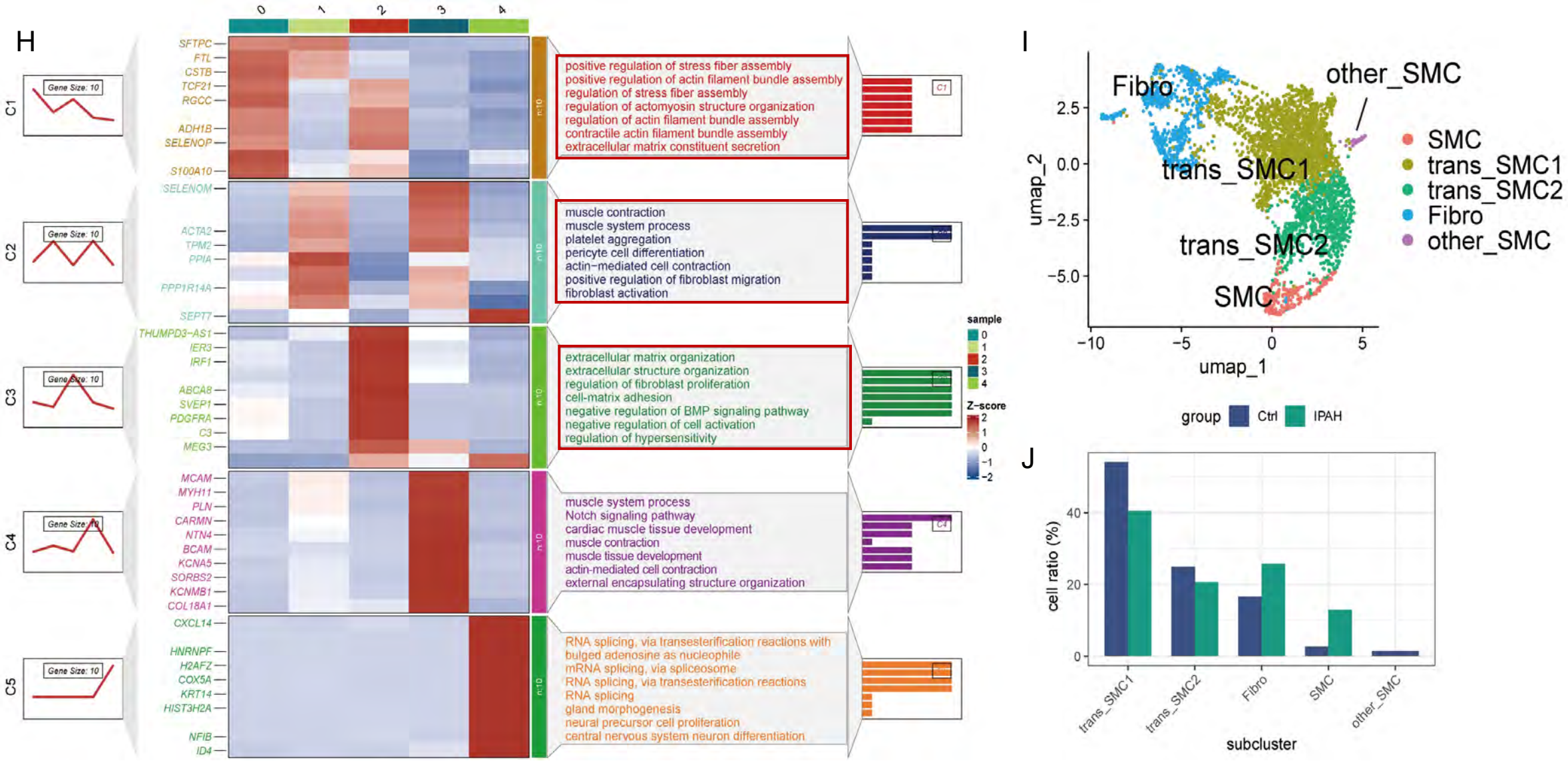

H
0
1
2
3
4
C1
Gene Size: 10
SFTPC
FTL
CSTB
TCF21
RGCC
ADH1B
SELENOP
S100A10
positive regulation of stress fiber assembly
positive regulation of actin filament bundle assembly
regulation of stress fiber assembly
regulation of actomyosin structure organization
regulation of actin filament bundle assembly
contractile actin filament bundle assembly
extracellular matrix constituent secretion
C2
Gene Size: 10
SELENOM
ACTA2
TPM2
PPIA
PPP1R14A
SEPT7
muscle contraction
muscle system process
platelet aggregation
pericyte cell differentiation
actin−mediated cell contraction
positive regulation of fibroblast migration
fibroblast activation
C3
Gene Size: 10
THUMPD3−AS1
IER3
IRF1
ABCA8
SVEP1
PDGFRA
C3
MEG3
extracellular matrix organization
extracellular structure organization
regulation of fibroblast proliferation
cell-matrix adhesion
negative regulation of BMP signaling pathway
negative regulation of cell activation
regulation of hypersensitivity
C4
Gene Size: 10
MCAM
MYH11
PLN
CARMN
NTN4
BCAM
KCNA5
SORBS2
KCNMB1
COL18A1
muscle system process
Notch signaling pathway
cardiac muscle tissue development
muscle contraction
muscle tissue development
actin-mediated cell contraction
external encapsulating structure organization
C5
Gene Size: 10
CXCL14
HNRNPF
H2AFZ
COX5A
KRT14
HIST3H2A
NFIB
ID4
RNA splicing, via transesterification reactions with bulged adenosine as nucleophile
mRNA splicing, via spliceosome
RNA splicing, via transesterification reactions
RNA splicing
gland morphogenesis
neural precursor cell proliferation
central nervous system neuron differentiation
n:10
sample
0
1
2
3
4
Z−score
2
1
0
−1
−2
I
Fibro
other_SMC
trans_SMC1
trans_SMC2
SMC
SMC
trans_SMC1
trans_SMC2
Fibro
other_SMC
umap_2
2.5
0.0
−2.5
−5.0
−10
−5
0
5
umap_1
group
Ctrl
IPAH
J
cell ratio (%)
40
20
0
trans_SMC1
trans_SMC2
Fibro
SMC
other_SMC
subcluster

Figure 2

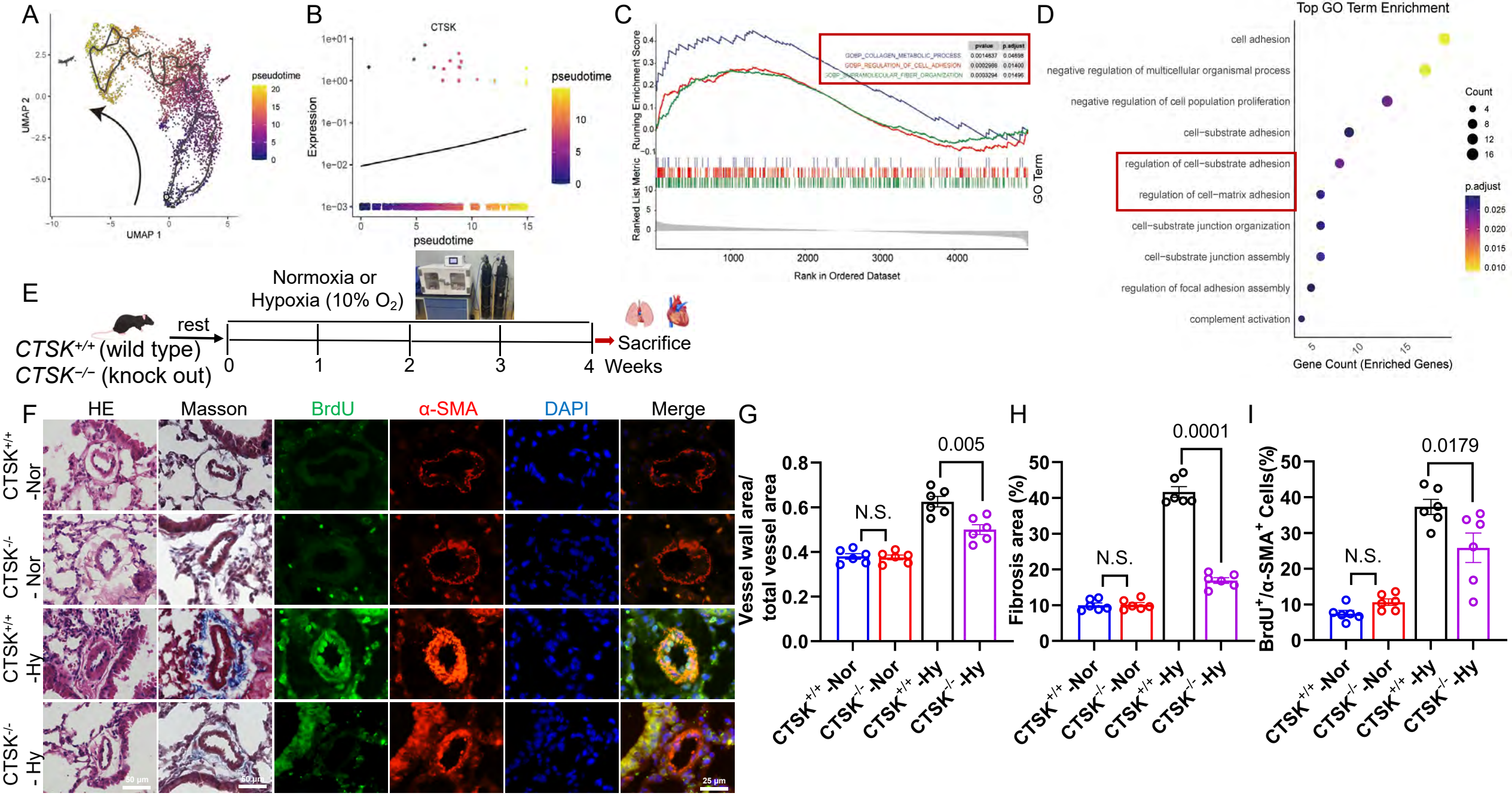

A
UMAP 2
UMAP 1
pseudotime
B
CTSK
Expression
pseudotime
C
Running Enrichment Score
Ranked List Metric
Rank in Ordered Dataset
GO Term
D
Top GO Term Enrichment
cell adhesion
negative regulation of multicellular organismal process
negative regulation of cell population proliferation
cell−substrate adhesion
regulation of cell−substrate adhesion
regulation of cell−matrix adhesion
cell−substrate junction organization
cell−substrate junction assembly
regulation of focal adhesion assembly
complement activation
Count
p.adjust
Gene Count (Enriched Genes)
E
Normoxia or
Hypoxia (10% O2)
rest
CTSK+/+ (wild type)
CTSK−/− (knock out)
0
1
2
3
4
Weeks
Sacrifice
F
HE
Masson
BrdU
α-SMA
DAPI
Merge
CTSK+/+ -Nor
CTSK-/- - Nor
CTSK+/+ -Hy
CTSK-/- - Hy
50 μm
25 μm
G
Vessel wall area/ total vessel area
N.S.
0.005
H
Fibrosis area (%)
N.S.
0.0001
I
BrdU+/α-SMA+ Cells(%)
N.S.
0.0179
CTSK+/+ -Nor
CTSK-/- -Nor
CTSK+/+ -Hy
CTSK-/- -Hy

Figure 2

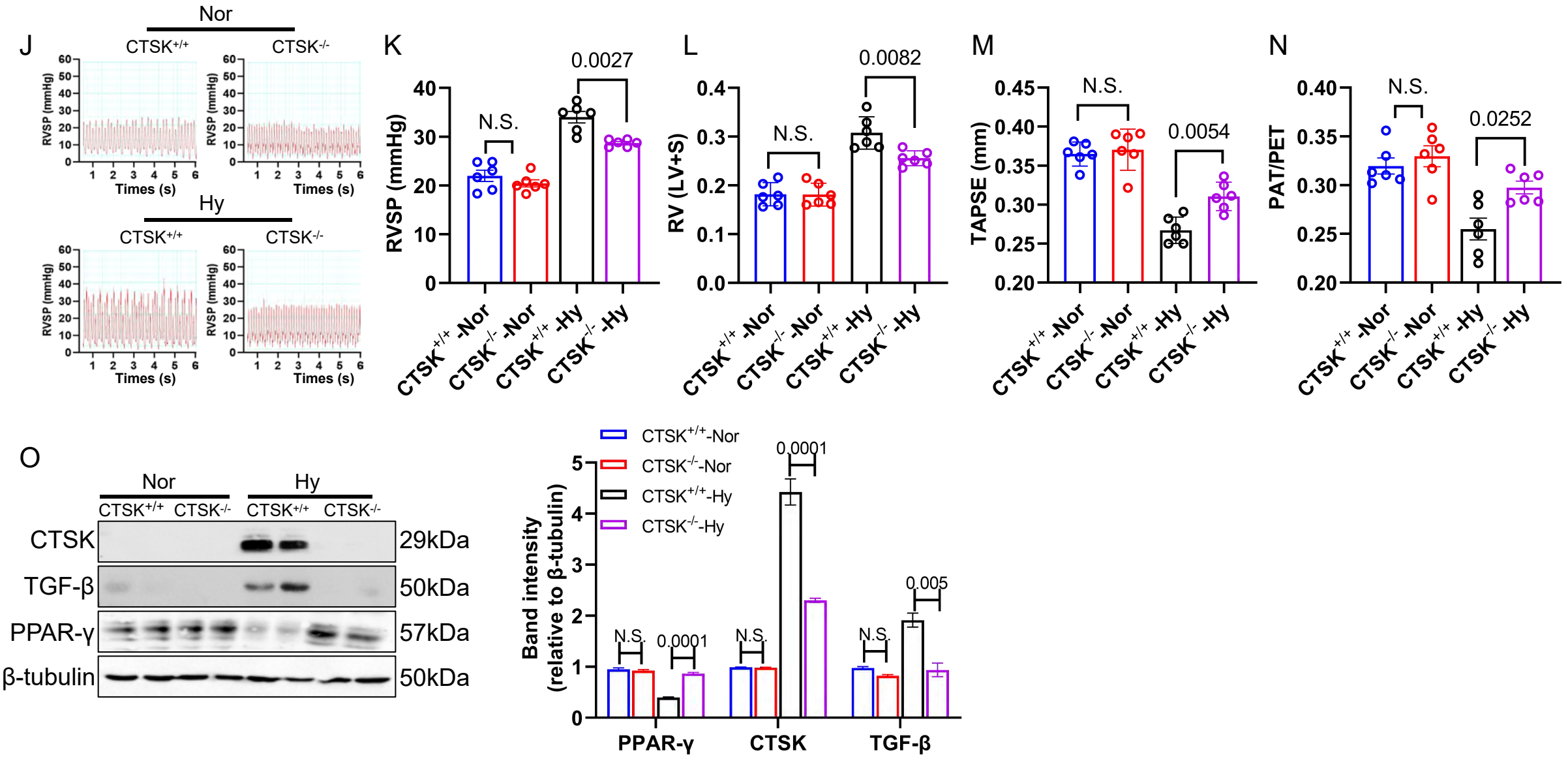
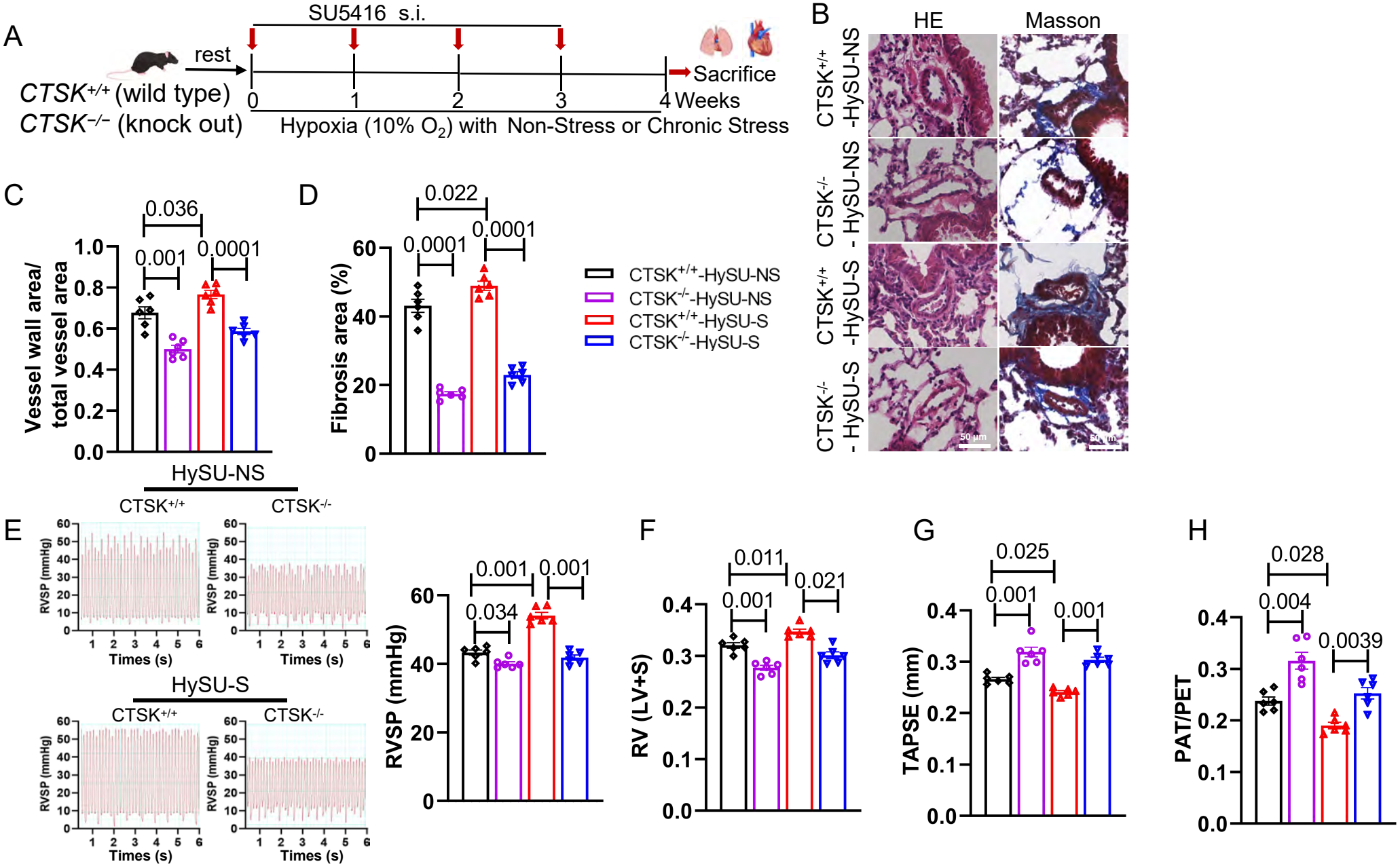

J
Nor
CTSK+/+
CTSK-/-
Hy
CTSK+/+
CTSK-/-
RVSP (mmHg)
Times (s)
K
RVSP (mmHg)
N.S.
0.0027
L
RV (LV+S)
N.S.
0.0082
M
TAPSE (mm)
N.S.
0.0054
N
PAT/PET
N.S.
0.0252
CTSK+/+ -Nor
CTSK-/- -Nor
CTSK+/+ -Hy
CTSK-/- -Hy
O
Nor
Hy
CTSK+/+
CTSK-/-
CTSK+/+
CTSK-/-
CTSK
TGF-β
PPAR-γ
β-tubulin
29kDa
50kDa
57kDa
50kDa
CTSK+/+-Nor
CTSK-/--Nor
CTSK+/+-Hy
CTSK-/--Hy
Band intensity (relative to β-tubulin)
N.S.
0.0001
N.S.
0.0001
N.S.
0.005
PPAR-γ
CTSK
TGF-β

Figure 3


A
SU5416 s.i.
rest
Sacrifice
CTSK+/+ (wild type)
CTSK−/− (knock out)
0
1
2
3
4 Weeks
Hypoxia (10% O2) with Non-Stress or Chronic Stress
B
HE
Masson
CTSK+/+ -HySU-NS
CTSK-/- - HySU-NS
CTSK+/+ -HySU-S
CTSK-/- - HySU-S
50 μm
C
Vessel wall area/ total vessel area
0.036
0.001
0.0001
HySU-NS
D
Fibrosis area (%)
0.022
0.0001
0.0001
CTSK+/+-HySU-NS
CTSK-/--HySU-NS
CTSK+/+-HySU-S
CTSK-/--HySU-S
E
CTSK+/+
CTSK-/-
RVSP (mmHg)
Times (s)
HySU-NS
HySU-S
RVSP (mmHg)
0.001
0.001
0.034
F
RV (LV+S)
0.011
0.001
0.021
G
TAPSE (mm)
0.025
0.001
0.001
H
PAT/PET
0.028
0.004
0.0039

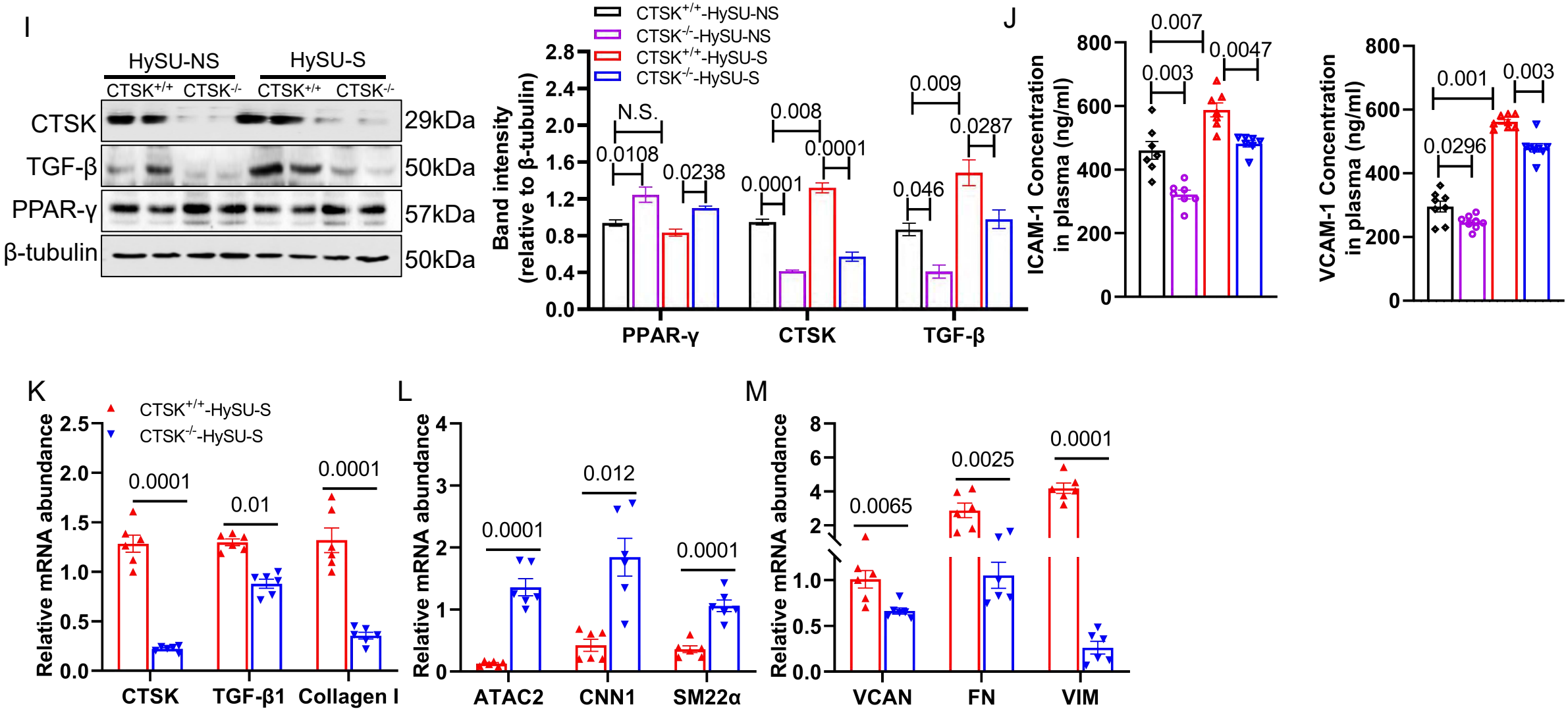

I
HySU-NS
HySU-S
CTSK+/+
CTSK-/-
CTSK+/+
CTSK-/-
CTSK
TGF-β
PPAR-γ
β-tubulin
29kDa
50kDa
57kDa
50kDa
CTSK+/+-HySU-NS
CTSK-/--HySU-NS
CTSK+/+-HySU-S
CTSK-/--HySU-S
Band intensity (relative to β-tubulin)
N.S.
0.0108
0.0238
0.008
0.0001
0.0001
0.009
0.0287
0.046
PPAR-γ
CTSK
TGF-β
J
ICAM-1 Concentration in plasma (ng/ml)
0.007
0.0047
0.003
VCAM-1 Concentration in plasma (ng/ml)
0.001
0.003
0.0296
K
CTSK+/+-HySU-S
CTSK-/--HySU-S
Relative mRNA abundance
0.0001
0.01
0.0001
CTSK
TGF-β1
Collagen I
L
Relative mRNA abundance
0.0001
0.012
0.0001
ATAC2
CNN1
SM22α
M
Relative mRNA abundance
0.0065
0.0025
0.0001
VCAN
FN
VIM

Figure 4

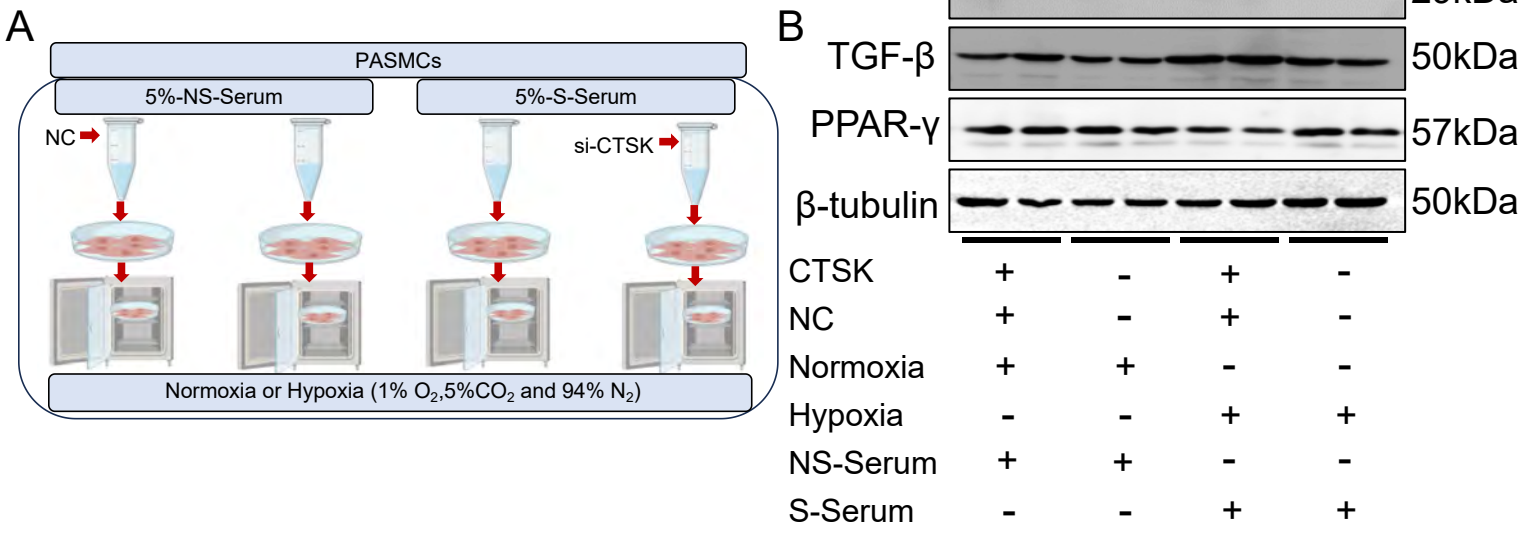
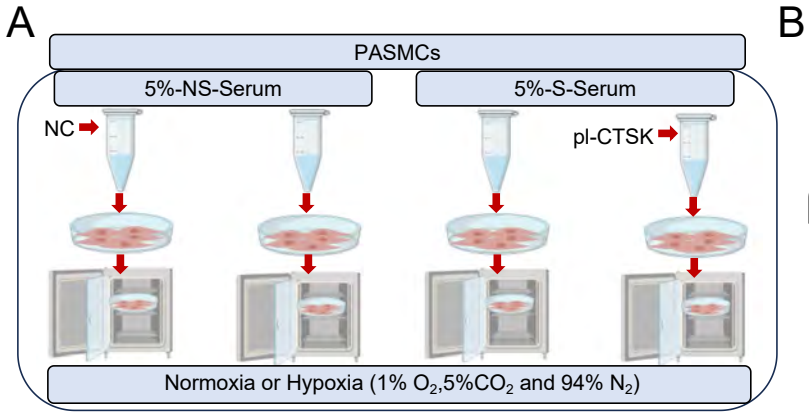
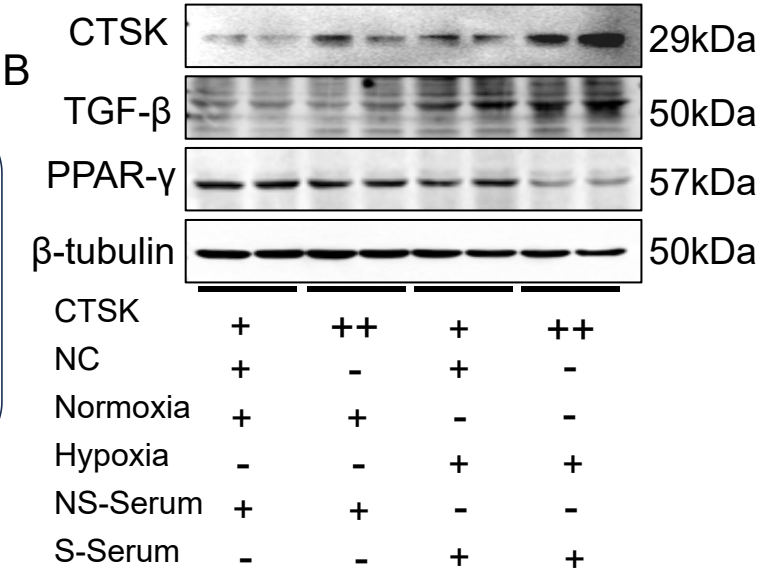
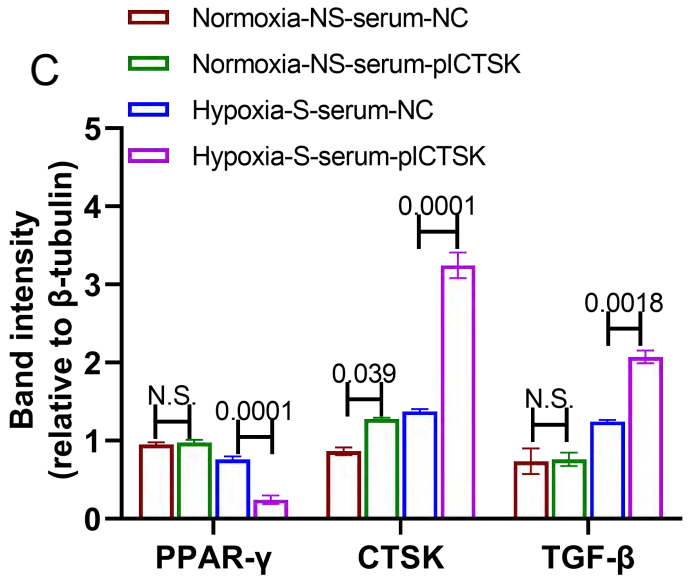
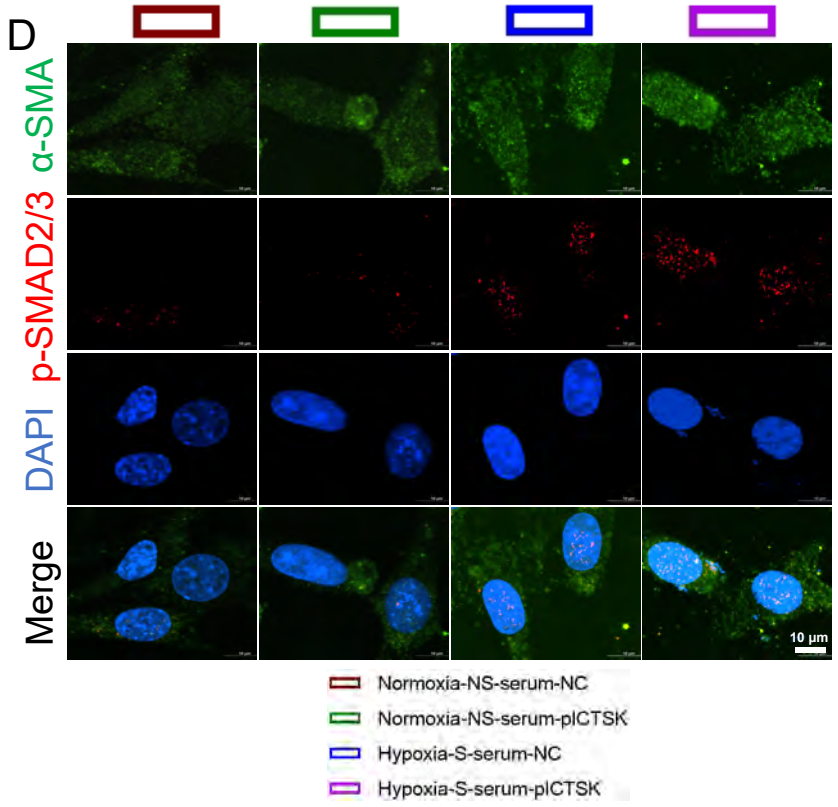

A
PASMCs
5%-NS-Serum
5%-S-Serum
NC
si-CTSK
Normoxia or Hypoxia (1% O2,5%CO2 and 94% N2)
B
CTSK
TGF-β
PPAR-γ
β-tubulin
29kDa
50kDa
57kDa
50kDa
CTSK + - + -
NC + - + -
Normoxia + + - -
Hypoxia - - + +
NS-Serum + + - -
S-Serum - - + +
C
Normoxia-NS-serum-NC
Normoxia-NS-serum-siCTSK
Hypoxia-S-serum-NC
Hypoxia-S-serum-siCTSK
Band intensity (relative to β-tubulin)
N.S.
0.0086
0.043
0.0029
N.S.
0.005
PPAR-γ
CTSK
TGF-β
D
α-SMA
p-SMAD2/3
DAPI
Merge
10 μm
E
α-SMA
Collagen I
DAPI
Merge
10 μm
Normoxia-NS-serum-NC
Normoxia-NS-serum-siCTSK
Hypoxia-S-serum-NC
Hypoxia-S-serum-siCTSK
F
Normoxia-NS-serum-NC
Normoxia-NS-serum-siCTSK
Hypoxia-S-serum-NC
Hypoxia-S-serum-siCTSK
Oxygen Consumption Rate (pmoles/min/Norm.Unit)
Time (minutes)

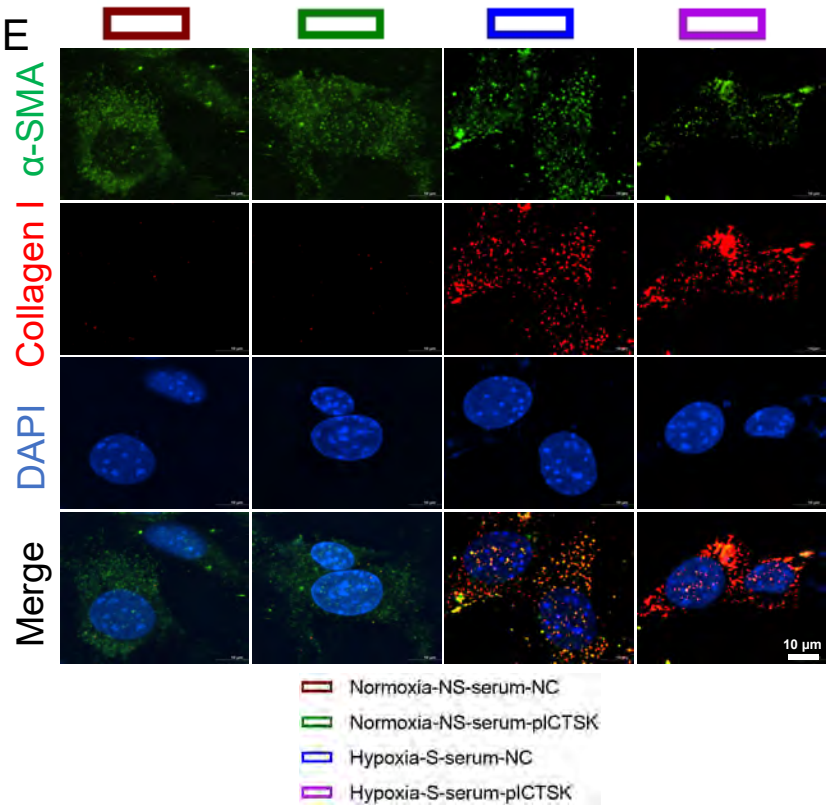
Figure 5


A
PASMCs
5%-NS-Serum
5%-S-Serum
NC
pl-CTSK
Normoxia or Hypoxia (1% O2,5%CO2 and 94% N2)


B
CTSK
TGF-β
PPAR-γ
β-tubulin
29kDa
50kDa
57kDa
50kDa
CTSK + ++ + ++
NC + - + -
Normoxia + + - -
Hypoxia - - + +
NS-Serum + + - -
S-Serum - - + +


C
Normoxia-NS-serum-NC
Normoxia-NS-serum-plCTSK
Hypoxia-S-serum-NC
Hypoxia-S-serum-plCTSK
Band intensity (relative to β-tubulin)
N.S.
0.0001
0.039
0.0001
N.S.
0.0018
PPAR-γ
CTSK
TGF-β


D
α-SMA
p-SMAD2/3
DAPI
Merge
10 μm
Normoxia-NS-serum-NC
Normoxia-NS-serum-plCTSK
Hypoxia-S-serum-NC
Hypoxia-S-serum-plCTSK


E
α-SMA
Collagen I
DAPI
Merge
10 μm
Normoxia-NS-serum-NC
Normoxia-NS-serum-plCTSK
Hypoxia-S-serum-NC
Hypoxia-S-serum-plCTSK

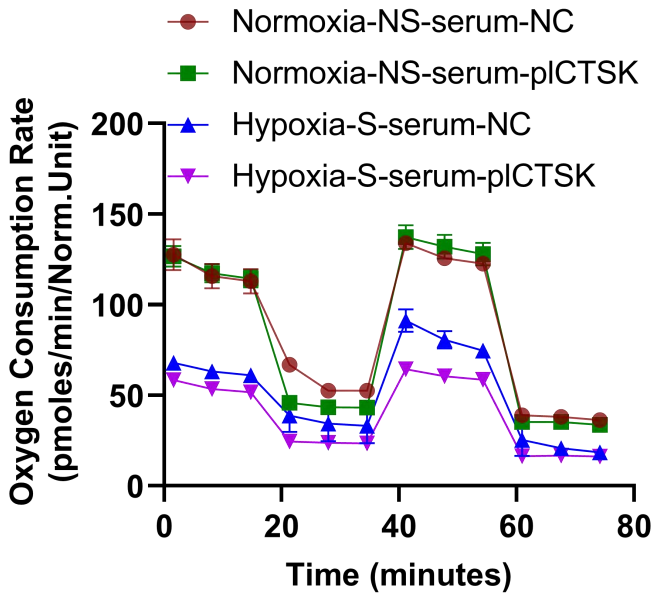

F
Normoxia-NS-serum-NC
Normoxia-NS-serum-plCTSK
Hypoxia-S-serum-NC
Hypoxia-S-serum-plCTSK
Oxygen Consumption Rate (pmoles/min/Norm.Unit)
Time (minutes)

Figure 6

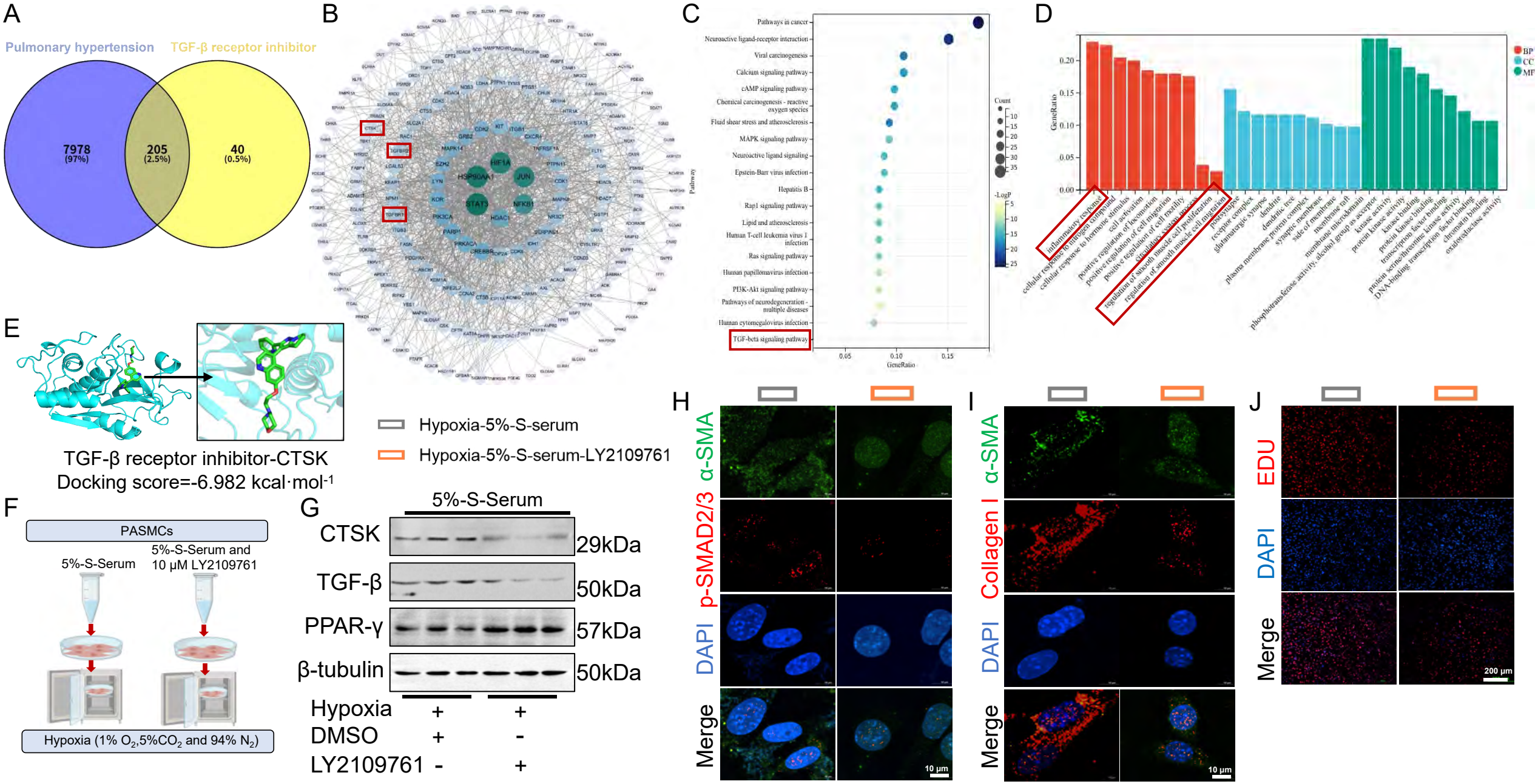
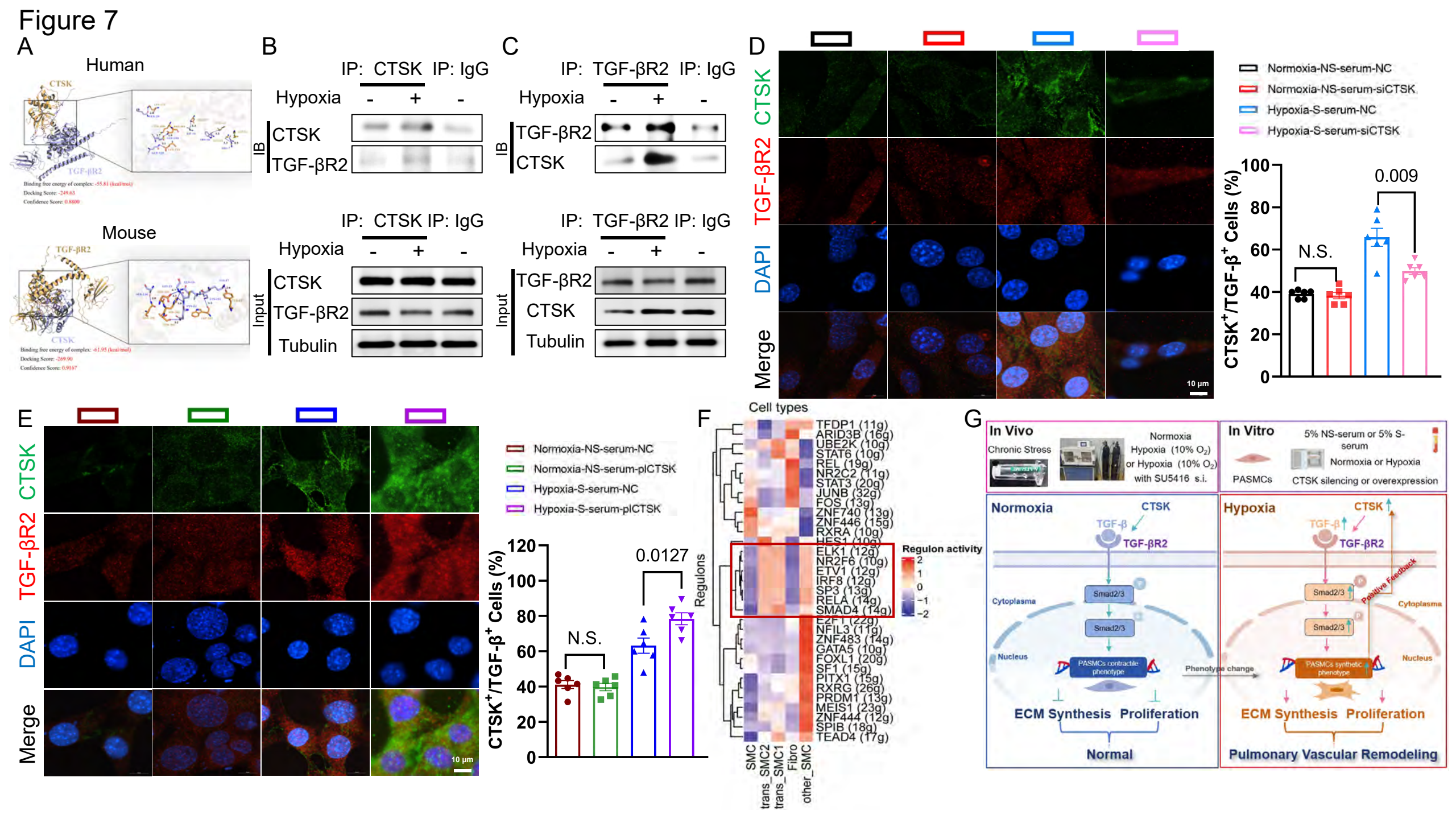

A
Pulmonary hypertension
TGF-β receptor inhibitor
7978
(97%)
205
(2.5%)
40
(0.5%)
B
C
Pathways in cancer
Neuroactive ligand-receptor interaction
Viral carcinogenesis
Calcium signaling pathway
cAMP signaling pathway
Chemical carcinogenesis - reactive oxygen species
Fluid shear stress and atherosclerosis
MAPK signaling pathway
Neuroactive ligand signaling
Epstein-Barr virus infection
Hepatitis B
Rap1 signaling pathway
Lipid and atherosclerosis
Human T-cell leukemia virus 1 infection
Ras signaling pathway
Human papillomavirus infection
PI3K-Akt signaling pathway
Pathways of neurodegeneration - multiple diseases
Human cytomegalovirus infection
TGF-beta signaling pathway
Pathway
GeneRatio
Count
-LogP
D
BP
CC
MF
GeneRatio
inflammatory response
cellular response to nitrogen compound
cellular response to hormone stimulus
positive regulation of cell activation
positive regulation of leukocyte migration
positive regulation of cell motility
regulation of smooth muscle cell proliferation
regulation of smooth muscle cell migration
postsynapse
receptor complex
glutamatergic synapse
dendrite
dendritic tree
plasma membrane protein complex
synaptic membrane
side of membrane
membrane raft
membrane microdomain
phosphotransferase activity, alcohol group as acceptor
kinase activity
protein kinase activity
kinase binding
protein kinase binding
transcription factor binding
protein serine/threonine kinase activity
DNA-binding transcription factor binding
chromatin binding
oxidoreductase activity
E
TGF-β receptor inhibitor-CTSK
Docking score=-6.982 kcal·mol-1
Hypoxia-5%-S-serum
Hypoxia-5%-S-serum-LY2109761
F
PASMCs
5%-S-Serum
5%-S-Serum and
10 μM LY2109761
Hypoxia (1% O2,5%CO2 and 94% N2)
G
5%-S-Serum
CTSK
29kDa
TGF-β
50kDa
PPAR-γ
57kDa
β-tubulin
50kDa
Hypoxia + +
DMSO + -
LY2109761 - +
H
α-SMA
p-SMAD2/3
DAPI
Merge
10 μm
I
α-SMA
Collagen I
DAPI
Merge
10 μm
J
EDU
DAPI
Merge
200 μm

Figure 7


A
Human
CTSK
TGF-βR2
Mouse
TGF-βR2
CTSK
B
IP: CTSK IP: IgG
Hypoxia - + -
IB
CTSK
TGF-βR2
Input
CTSK
TGF-βR2
Tubulin
C
IP: TGF-βR2 IP: IgG
Hypoxia - + -
IB
TGF-βR2
CTSK
Input
TGF-βR2
CTSK
Tubulin
D
CTSK
TGF-βR2
DAPI
Merge
10 μm
Normoxia-NS-serum-NC
Normoxia-NS-serum-siCTSK
Hypoxia-S-serum-NC
Hypoxia-S-serum-siCTSK
CTSK+/TGF-β+ Cells (%)
N.S.
0.009
E
CTSK
TGF-βR2
DAPI
Merge
10 μm
Normoxia-NS-serum-NC
Normoxia-NS-serum-plCTSK
Hypoxia-S-serum-NC
Hypoxia-S-serum-plCTSK
CTSK+/TGF-β+ Cells (%)
N.S.
0.0127
F
Cell types
Regulons
TFDP1 (11g)
ARID3B (16g)
UBE2K (10g)
STAT6 (10g)
REL (19g)
NR2C2 (11g)
STAT3 (20g)
JUNB (32g)
FOS (13g)
ZNF740 (13g)
ZNF446 (15g)
RXRA (10g)
HES1 (10g)
ELK1 (12g)
NR2F6 (10g)
ETV1 (12g)
IRF8 (12g)
SP3 (13g)
RELA (14g)
SMAD4 (14g)
E2F1 (22g)
NFIL3 (11g)
ZNF483 (14g)
GATA5 (10g)
FOXL1 (20g)
SF1 (15g)
PITX1 (15g)
RXRG (26g)
PRDM1 (13g)
MEIS1 (23g)
ZNF444 (12g)
SPIB (18g)
TEAD4 (17g)
SMC
trans_SMC2
trans_SMC1
Fibro
other_SMC
Regulon activity
G
In Vivo
Chronic Stress
Normoxia
Hypoxia (10% O2)
or Hypoxia (10% O2)
with SU5416 s.i.
In Vitro
PASMCs
5% NS-serum or 5% S-serum
Normoxia or Hypoxia
CTSK silencing or overexpression
Normoxia
CTSK
TGF-β
TGF-βR2
Smad2/3
Cytoplasma
Nucleus
PASMCs contractile phenotype
Phenotype change
ECM Synthesis Proliferation
Normal
Hypoxia
CTSK
TGF-β
TGF-βR2
Positive Feedback
Smad2/3
Cytoplasma
Nucleus
PASMCs synthetic phenotype
ECM Synthesis Proliferation
Pulmonary Vascular Remodeling

1

## Supplementary Files

This is a list of supplementary files associated with this preprint. Click to download.

- FullluneditedgelWBDrZhang.pdf
- SupplementaryData.pdf